

The anatomy of the Orion B giant molecular cloud: A local template for studies of nearby galaxies

Jérôme Pety^{1,2}, Viviana V. Guzmán^{3,4}, Jan H. Orkisz^{5,1,2}, Harvey S. Liszt⁶, Maryvonne Gerin²,
Emeric Bron^{7,9}, Sébastien Bardeau¹, Javier R. Goicoechea⁹, Pierre Gratier⁸, Franck Le Petit⁷,
François Levrier², Karin I. Öberg³, Evelyne Roueff⁷, and Albrecht Sievers¹⁰

¹ IRAM, 300 rue de la Piscine, 38406 Saint-Martin-d'Hères, France

e-mail: pety@iram.fr

² LERMA, Observatoire de Paris, PSL Research University, CNRS, Sorbonne Universités, UPMC Univ. Paris 06,
École normale supérieure, 75005 Paris, France

³ Harvard-Smithsonian Center for Astrophysics, 60 Garden Street, Cambridge, MA, 02138, USA

⁴ Joint ALMA Observatory (JAO), Alonso de Cordova 3107 Vitacura, Santiago de Chile, Chile

⁵ Univ. Grenoble Alpes, IRAM, 38000 Grenoble, France

⁶ National Radio Astronomy Observatory, 520 Edgemont Road, Charlottesville, VA, 22903, USA

⁷ LERMA, Observatoire de Paris, PSL Research University, CNRS, Sorbonne Universités, UPMC Univ. Paris 06, 92190 Meudon,
France

⁸ Laboratoire d'Astrophysique de Bordeaux, Univ. Bordeaux, CNRS, B18N, allée Geoffroy Saint-Hilaire, 33615 Pessac, France

⁹ ICMM, Consejo Superior de Investigaciones Científicas (CSIC), 28049 Madrid, Spain

¹⁰ IRAM, Avenida Divina Pastora, 7, Núcleo Central, 18012 Granada, España

Received 7 October 2016 / Accepted 8 November 2016

ABSTRACT

Context. Molecular lines and line ratios are commonly used to infer properties of extra-galactic star forming regions. The new generation of millimeter receivers almost turns every observation into a line survey. Full exploitation of this technical advancement in extra-galactic study requires detailed bench-marking of available line diagnostics.

Aims. We aim to develop the Orion B giant molecular cloud (GMC) as a local template for interpreting extra-galactic molecular line observations.

Methods. We use the wide-band receiver at the IRAM-30 m to spatially and spectrally resolve the Orion B GMC. The observations cover almost 1 square degree at 26'' resolution with a bandwidth of 32 GHz from 84 to 116 GHz in only two tunings. Among the mapped spectral lines are the ¹²CO, ¹³CO, C¹⁸O, C¹⁷O, HCN, HNC, ¹²CN, C₂H, HCO⁺, N₂H⁺ (1–0), and ¹²CS, ³²SO, SiO, c-C₃H₂, CH₃OH (2–1) transitions.

Results. We introduce the molecular anatomy of the Orion B GMC, including relationships between line intensities and gas column density or far-UV radiation fields, and correlations between selected line and line ratios. We also obtain a dust-traced gas mass that is less than approximately one third the CO-traced mass, using the standard X_{CO} conversion factor. The presence of over-luminous CO can be traced back to the dependence of the CO intensity on UV illumination. As a matter of fact, while most lines show some dependence on the UV radiation field, CN and C₂H are the most sensitive. Moreover, dense cloud cores are almost exclusively traced by N₂H⁺. Other traditional high-density tracers, such as HCN(1–0), are also easily detected in extended translucent regions at a typical density of $\sim 500 \text{ H}_2 \text{ cm}^{-3}$. In general, we find no straightforward relationship between line critical density and the fraction of the line luminosity coming from dense gas regions.

Conclusions. Our initial findings demonstrate that the relationships between line (ratio) intensities and environment in GMCs are more complicated than often assumed. Sensitivity (i.e., the molecular column density), excitation, and, above all, chemistry contribute to the observed line intensity distributions, and they must be considered together when developing the next generation of extra-galactic molecular line diagnostics of mass, density, temperature, and radiation field.

Key words. galaxies: ISM – ISM: clouds – HII regions – radio lines: galaxies – astrochemistry

1. Introduction

The star formation process from interstellar gas raises many outstanding questions. For instance, the relative roles of micro-physics and galactic environment on star formation efficiency are debated; more precisely, the respective roles of magnetic fields, self-gravity, and turbulence (see e.g., Hennebelle & Chabrier 2011; Hennebelle 2013) compared with the external pressure, position in galactic spiral arm/interarm regions and spiral-arm streaming motions (e.g., Meidt et al. 2013; Hughes et al. 2013).

Other points hotly discussed include the impact of feedback from H II region expansion and supernovae (Kim et al. 2013), the identification of the key dynamical parameters (Mach number, virial parameter, amount of energy in solenoidal/compressive modes of the turbulence, see Federrath & Klessen 2012, 2013, for example), the amount of CO-dark molecular gas and whether this biases global estimation of the mass of the molecular reservoir at cloud scales (Wolfire et al. 2010; Liszt & Pety 2012), the relative fractions of diffuse ($\sim 100\text{--}500 \text{ cm}^{-3}$, 80 K) and dense ($\sim 10^4 \text{ cm}^{-3}$, 10 K) gas in a giant molecular cloud (GMC), and

the determination of the true fraction of star-forming dense gas (Lada et al. 2010, 2012, 2013).

All these questions also arise in extra-galactic studies with the additional difficulty that GMCs are unresolved at the typically achieved angular resolution ($1''$ corresponds to 15 pc for a 3 Mpc distant galaxy). It is therefore crucial to first understand how the average spectra of molecular lines relate to actual physical properties when the line emission is spatially resolved. By mapping a significant fraction of a GMC at a spatial resolution of ~ 50 mpc and a spectral resolution of 0.6 km s^{-1} , we address some of the following issues: what linear resolution must be achieved on a GMC to correctly derive its global properties including star formation rate and efficiency (Leroy et al. 2016)? For instance, are usual extra-galactic line tracers of the various molecular cloud density regimes reliable (Bigiel et al. 2016)? Do we get a more accurate estimate of the mass by resolving the emission? More generally, can we derive empirical laws that link tracer properties averaged over a GMC to its internal star-forming activity?

With the advent of wide-bandwidth receivers associated to high-resolution spectrometers, any observation now simultaneously delivers emission from many different tracers. Moreover, the increased sensitivity makes it possible to cover large fields of view (FoVs). The possibility to map many different lines in many different environments allows us to start answering the questions presented above. The essence of the ORION-B (Outstanding Radio Imaging of Orion B, PI: J. Pety) project is to recast the science questions of star formation in a statistical way. Wide-field hyper-spectral mapping of Orion B is used to obtain an accurate 3D description of the molecular structure in a GMC, a key for defining chemical probes of the star-formation activity in more distant Galactic and extragalactic sources.

Approximately thirty 3 mm lines are detected in only two frequency tunings with the same sensitive radio single-dish telescope at a typical resolution of $26''$ over almost 1 square degree. The field of view (5.6×7.5 pc) would fall in a single resolution element of a map of the Orion B molecular cloud observed at 3 mm with a telescope of similar diameter as the IRAM-30 m from the Small or Large Magellanic Clouds. The spectra, averaged over the field of view, would then represent the spectra of Orion B as seen by an alien from the Magellanic Clouds. Conversely, our imaging experiment allows us to reveal the detailed anatomy of a molecular emission that is usually hidden behind these mean spectra in nearby galaxy studies. The south-western edge of the Orion B molecular cloud (a.k.a. Barnard 33 or Lynds 1630) represents an ideal laboratory for this kind of study. It forms both low-mass and massive stars, and contains regions of triggered or spontaneous star formation, photon-dominated regions and UV-shielded cold gas, all in a single source.

In companion papers, Gratier et al. (2017) study a Principal Component Analysis (PCA) of the same dataset to understand the main correlations that exist between the different lines. Orkisz et al. (2017) quantify the fractions of turbulent energy that are associated with the solenoidal/compressive modes, and they relate these values to the star formation efficiency in Orion B. In this paper, we present the observational results of the ORION-B project, focusing on the mean properties of this GMC and evaluate the diagnostic power of commonly used line tracers and ratios.

We present the targeted field of view, as well as the observations and data reduction process in Sect. 2. Typical properties such as UV-illumination, mean line profiles, CO-traced, dust-traced and virial masses are computed in Sect. 3. In Sect. 4, we investigate the fraction of flux arising in different gas regimes

for each line. In Sect. 5, we compare the visual extinction map with the line integrated intensities and compute the luminosity per proton of the different line tracers. The properties of various line ratios are discussed in Sect. 6. A discussion is presented in Sect. 7, focusing on possible biases introduced by the characteristics of the observed field of view, and whether the HCO⁺, HCN, and HNC (1–0) lines are good tracers of dense gas. We end the discussion by comparing the observed line ratios in Orion B with extra-galactic observation results. Section 8 summarizes the results and concludes the paper.

2. The Orion B GMC

2.1. Targeted field of view

Figure 1 displays a composite image of the ^{12}CO (blue), ^{13}CO (green), and C^{18}O (red) (1–0) peak-intensity main-beam temperatures. It shows the south-western edge of the Orion B molecular cloud. This region samples the interaction of the molecular cloud with at least four H II regions. First, σOri is an O9.5V star that illuminates the western edge of the Orion B cloud. It creates the IC 434 nebula from which the Horsehead pillar emerges. Second, NGC 2023 and NGC 2024 are two younger H II regions embedded in the Orion B molecular cloud, powered by B1.5V (HD 37903) or late O, early B (IRS2b) stars, respectively (Bik et al. 2003). NGC 2024 covers 20 arcmin at the northern edge of the mapped FoV, while NGC 2023 is situated approximately halfway between IRS2b and the Horsehead. The B5V HD 38087 star creates the IC 435 nebula at the south-eastern edge of the FoV. Finally, one of the three Orion Belt stars, the O9.71b star Alnitak (a.k.a. ζOri), falls in the observed FoV. Table 1 lists the characteristics of these exciting stars. To guide the eye on the right panel of Fig. 1, we overlaid crosses at the position of the main exciting stars, and circles at the approximate boundaries of the different H II regions. These visual markers are used throughout the paper.

2.2. IRAM-30 m observations

The observations were taken with the IRAM-30 m telescope in four observing runs: August 2013, December 2013, August 2014, and November 2014 for 133 h in total (telescope time) under average summer weather (6 mm median water vapor) and good winter weather (3 mm median water vapor). During all these runs, we observed with a combination of the 3 mm sideband separated EMIR receivers and the Fourier transform spectrometers, which yields a total bandwidth of ~ 32 GHz per tuning (i.e., ~ 8 GHz per sideband and per polarization) at a channel spacing of 195 kHz or $0.5\text{--}0.7 \text{ km s}^{-1}$. The two tuned frequencies were 102.519 GHz and 110.000 GHz at the 6.25 MHz intermediate frequency of the upper sideband, resulting in local oscillator frequencies of 96.269 and 103.750 GHz, respectively. This allowed us to observe nearly the entire 3 mm band from 84.5 to 116.5 GHz.

We used the on-the-fly scanning strategy with a dump time of 0.25 s and a scanning speed of $17''/\text{s}$ to ensure a sampling of five dumps per beam along the scanning direction at the $21.2''$ resolution reached at the highest observed frequency, that is, 116 GHz. We covered the full FoV (~ 0.9 square degrees) with 103 tiles of approximately $110'' \times 1000''$ size. The rectangular tiles had a position angle of 14° in the Equatorial J2000 frame to adapt the mapping strategy to the global morphology of the western edge of the Orion B molecular cloud. These tiles were covered with rasters along their long axis (almost the Dec direction). The

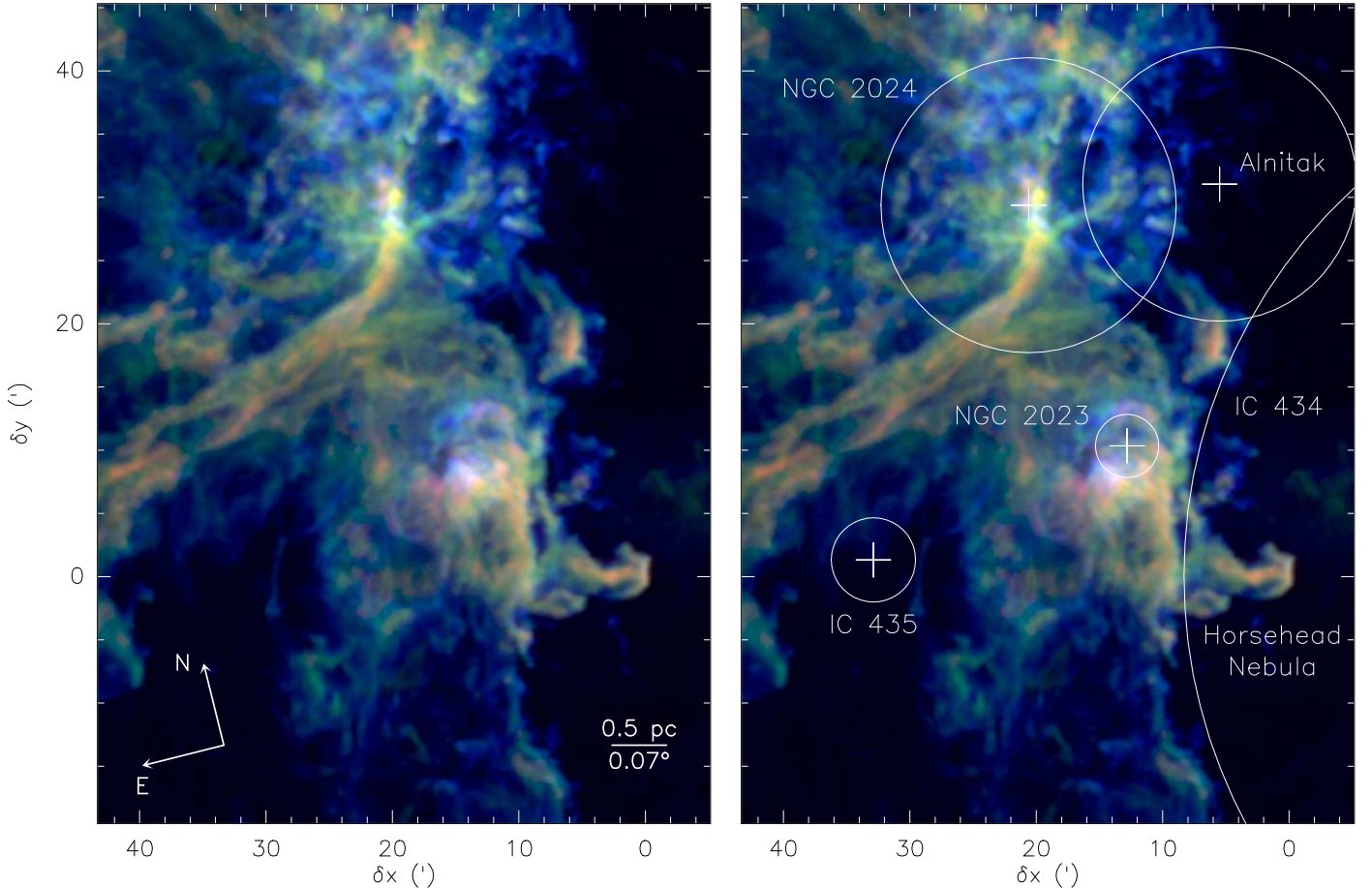


Fig. 1. Composite image of the ^{12}CO (blue), ^{13}CO (green), C^{18}O (red) (1–0) peak-intensity main-beam temperature. The circles show the typical extensions of the H II regions and the crosses show the position of the associated exciting stars (see Table 1). The σ -Ori star that excites the IC 434 H II region is located 0.5° east of the Horsehead nebula.

Table 1. Properties of the stars exciting the H II regions in the observed field of view.

H II region	Star	Type	α, δ (J2000)	$(\delta x, \delta y)$ (", ")	Parallax mas	Distance pc	V_{LSR} km s^{-1}
IC 434	σ Ori	O9.5V B	05 ^h 38 ^m 44.779 ^s , -02°36'00.12"	(-33.35, 00.07)	$2.5806 \pm 0.0088^{(1)}$	$387.5 \pm 1.3^{(1)}$	15.0 ± 1.6
IC 435	HD 38087	B5V D	05 ^h 43 ^m 00.573 ^s , -02°18'45.38"	(+32.87, 01.33)	$5.90 \pm 1.29^{(2)}$	$169 \pm 37^{(2)}$	18.1 ± 4.5
NGC 2023	HD 37903	B1.5V C	05 ^h 41 ^m 38.388 ^s , -02°15'32.48"	(+13.72, 09.42)	$2.776 \pm 0.271^{(3)}$	$362 \pm 35^{(3)}$	-7.7 ± 2
NGC 2024	IRS2b	O8V-B2V	05 ^h 41 ^m 45.50 ^s , -01°54'28.7"	(+20.54, 29.43)	—	415 ⁽⁴⁾	—
	Alnitak	O9.7Ib+B0III C	05 ^h 40 ^m 45.527 ^s , -01°56'33.26"	(+05.49, 31.04)	$3.4 \pm 0.2^{(5)}$	$294 \pm 21^{(5)}$	3.7 ± 1.3

Notes. ⁽¹⁾ Schaefer et al. (2016); ⁽²⁾ van Leeuwen (2007); ⁽³⁾ Gaia DR1: Gaia Collaboration (2016b), Lindegren et al. (2016), Fabricius et al. (2016), Gaia Collaboration (2016a); ⁽⁴⁾ Anthony-Twarog (1982); ⁽⁵⁾ Hummel et al. (2013).

separation between two successive rasters was $\lambda/2D = 8.46''$ to ensure Nyquist sampling perpendicular to the scanning direction. The scanning direction was reversed at the end of each line (zigzag mode). This implied a tongue and groove shape at the bottom and top part of each tile. We thus overlapped the top and bottom edges of the tiles by $30''$ to ensure correct sampling. Furthermore, the left and right edges of the tiles were adjusted to avoid any overlap, that is, to maximize the overall scanning speed. The FoV was covered only once by the telescope, except for the tiles observed in the worst conditions (low elevation and/or bad weather) that were repeated once.

The calibration parameters (including the system temperature) were measured every 15 min. The pointing was checked every two hours and the focus every four hours. Following Mangum et al. (2007) and Pety et al. (2009), we used the

optimum position switching strategy. A common off reference position was observed for 11 s every 59 s with the following repeated sequence OFF-OTF-OTF-OFF, where OFF is the reference position and OTF stands for On-The-Fly. No reference position completely devoid of ^{12}CO (1–0) emission could be localized in the close neighborhood of the Orion B western edge. As this reference position is subtracted from every OTF spectrum in order to remove the common atmospheric contribution, the presence of signal in the reference position results in a spurious negative contribution to the signal everywhere in the final cube. Searching for a reference position farther away in the hope that it is devoid of signal would degrade the quality of the baseline because the atmospheric contribution would vary from the OTF spectra to the reference position. We thus tested several nearby potential reference positions using the

Table 2. Typical properties of the south-western edge of Orion B.

Parameter	Value	Notes
Distance	400 pc	$1'' = 2 \text{ mpc}$
Systemic velocity	10.5 km s^{-1}	LSR, radio convention
Projection center	$05^{\text{h}}40^{\text{m}}54.270^{\text{s}}, -02^{\circ}28'00.00''$	$\alpha, \delta(\text{J2000})$, mane of the Horsehead
Offset range and field of view	$[-5.2', +43.3'] \times [-19.5', 45.3']$	$49' \times 65'$ or $5.6 \times 7.5 \text{ pc}$
$W_{\text{CO}}^{\text{min}} - W_{\text{CO}}^{\text{mean}} - W_{\text{CO}}^{\text{max}}$	$0 - 61 - 288 \text{ K km s}^{-1}$	in $[-2, +18] \text{ km s}^{-1}$
$A_V^{\text{min}} - A_V^{\text{mean}} - A_V^{\text{max}}$	$0.7 - 4.7 - 222 \text{ mag}$	$A_K/A_V = 0.13$
$T_d^{\text{min}} - T_d^{\text{mean}} - T_d^{\text{max}}$	$16 - 26 - 99 \text{ K}$	
$G_0^{\text{min}} - G_0^{\text{mean}} - G_0^{\text{max}}$	$4 - 45 - 36\,000$	Inter-Stellar Radiation Field (Habing 1968)
CO-traced mass	$11\,000 M_{\odot}$	Standard X_{CO} and helium dealt with
Dust-traced mass	$3\,900 M_{\odot}$	Standard N_{H}/A_V and H I gas negligible
Virial traced mass	Between $6\,200$ and $9\,500 M_{\odot}$	Depending on the assumed density radial profile
Imaged surface	43 pc^2	$= S$
Typical volume	280 pc^3	$= S^{3/2}$
CO-traced mean column density	$260 M_{\odot} \text{ pc}^{-2} 12 \times 10^{21} \text{ H}_2 \text{ cm}^{-2}$	Standard X_{CO} and helium dealt with
Dust-traced mean column density	$92 M_{\odot} \text{ pc}^{-2} 4 \times 10^{21} \text{ H}_2 \text{ cm}^{-2}$	Standard N_{H}/A_V and H I gas negligible
CO-traced mean volume density	$40 M_{\odot} \text{ pc}^{-3} 590 \text{ H}_2 \text{ cm}^{-3}$	Standard X_{CO} and helium dealt with
Dust-traced mean volume density	$14 M_{\odot} \text{ pc}^{-3} 210 \text{ H}_2 \text{ cm}^{-3}$	Standard N_{H}/A_V and H I gas negligible

frequency-switched observing mode that does not require a reference position. This is possible because the observed lines have narrow linewidth. We then selected the nearest position that has the minimum line integrated emission in ^{12}CO (1–0). Offsets of this position are ($-500'', -500''$) with respect to the projection center given in Table 2. The ^{12}CO , and ^{13}CO (1–0) peak intensities at this position are ~ 1 and 0.05 K , respectively. The correction of the negative contribution from the reference position to the final cube requires a good observation of the reference position. We therefore observed this reference position using the frequency-switched observing mode in both tunings, a few minutes per observing session.

2.3. IRAM-30 m data reduction

Data reduction was carried out using the GILDAS¹/CLASS software. The data were first calibrated to the T_{A}^* scale using the chopper-wheel method (Penzias & Burrus 1973) before being converted to main-beam temperatures (T_{mb}) using the forward and main-beam efficiencies (F_{eff} and B_{eff}) listed in Table A.1. The B_{eff} values are derived from the Ruze's formula

$$B_{\text{eff}}(\lambda) = B_{\text{eff}}^0 \exp \left\{ - \left(\frac{4\pi\sigma}{\lambda} \right)^2 \right\}, \quad (1)$$

$$\text{with } B_{\text{eff}}^0 = 0.863, \quad \text{and } \sigma = 65.6 \mu\text{m}, \quad (2)$$

where λ presents the wavelength dependence². The resulting amplitude accuracy is $\sim 10\%$. A 12 to 20 MHz-wide subset of the spectra was first extracted around each line rest frequency. We computed the observed noise level after subtracting a first order baseline from every spectrum, excluding the velocity range from 0 to 18 km s^{-1} LSR, where the gas emits for all observed lines, except ^{12}CO and HCO^+ (1–0) for which the excluded velocity range was increased from -5 to 20 km s^{-1} LSR. A systematic

comparison of this noise value with the theoretical noise computed from the system temperature, the integration time, and the channel width allowed us to filter out outlying spectra (typically 3% of the data).

To correct for the negative contribution from the reference position to the final cube, we first averaged all the observations of the reference position 1) to increase the signal-to-noise ratio of the measured profiles, and 2) to decrease the influence of potential calibration errors. Signal in the reference position was only detected for the ^{12}CO and ^{13}CO (1–0) lines. The correction was thus applied only for these two lines. The averaged spectra at these frequencies were fitted by a combination of Gaussians after baseline subtraction, in order to avoid adding supplementary noise in the final cube. This fit was then added to every on-the-fly spectrum.

The spectra were then gridded into a data cube through a convolution with a Gaussian kernel of $FWHM \sim 1/3$ of the IRAM-30 m telescope beamwidth at the rest line frequency. To facilitate comparison of the different line cubes, we used the same spatial (pixels of $9''$ size) and spectral (80 channels spaced by 0.5 km s^{-1}) grid. The position-position-velocity cubes were finally smoothed at the common angular resolution of $31''$ to avoid resolution effects.

2.4. Map of visual extinction and dust temperature from Herschel and Planck data

In this paper, we observationally check the potential of line intensities and of ratios of line intensities to characterize physical properties of the emitting gas. Ancillary data are thus needed to deliver independent estimates of these physical properties. We use recent dust continuum observations to provide estimates of the column density of material and of the far UV illumination.

After combining the *Herschel* Gould Belt Survey (André et al. 2010; Schneider et al. 2013) and *Planck* observations (Planck Collaboration I 2011) in the direction of Orion B, Lombardi et al. (2014) fitted the spectral energy distribution to yield a map of dust temperature and a map of dust opacity at $850 \mu\text{m}$ (τ_{850}). Hollenbach et al. (1991) indicates that the equilibrium dust temperature at the slab surface of a 1D

¹ See <http://www.iram.fr/IRAMFR/GILDAS> for more information about the GILDAS softwares (Pety 2005).

² The values of B_{eff}^0 and σ can be found at <http://www.iram.es/IRAMES/mainWiki/Iram30mEfficiencies>

Table 3. Line intensities and luminosities in the $[-2, +18 \text{ km s}^{-1}]$ velocity range and including all pixels.

Species	Simplified ^a quantum numbers	Complete ^b quantum numbers	A_{ij} s^{-1}	E_u/k K	Intensity mK km s^{-1}	Relative to ^{12}CO	Luminosity L_\odot
^{12}CO	1–0	$J = 1–0$	7.2×10^{-8}	5.5	60 430	100.00	1.0×10^{-2}
^{13}CO	1–0	$J = 1–0$	3.2×10^{-8}	5.3	9 198	15.22	1.4×10^{-3}
HCO^+	1–0	$J = 1–0$	4.2×10^{-5}	4.3	1 630	2.70	1.3×10^{-4}
HCN	1–0	$J = 1–0, F = 2–1$	2.4×10^{-5}	4.3	1 540	2.55	1.2×10^{-4}
CN	1–0	$N = 1–0, J = 3/2–1/2, F = 5/2 – 3/2$	1.2×10^{-5}	5.4	776	1.28	1.3×10^{-4}
C^{18}O	1–0	$J = 1–0$	6.3×10^{-8}	5.3	556	0.92	8.0×10^{-5}
^{12}CS	2–1	$J = 2–1$	1.7×10^{-5}	7.0	513	0.85	5.3×10^{-5}
C_2H	1–0	$N = 1–0, J = 3/2–1/2, F = 2–1$	1.5×10^{-6}	4.2	457	0.76	3.2×10^{-5}
HNC	1–0	$J = 1–0, F = 2–1$	2.7×10^{-5}	4.4	445	0.74	3.6×10^{-5}
^{32}SO	2–1	$J = 3–2, K = 2–1$	1.1×10^{-5}	9.2	283	0.47	3.0×10^{-5}
C^{17}O	1–0	$J = 1–0, F = 7/2 – 5/2$	6.7×10^{-8}	5.4	215	0.36	3.3×10^{-5}
c- C_3H_2	2–1	$J = 2–1, K_+ = 1–0, K_- = 2–1$	2.3×10^{-5}	6.4	149	0.25	1.1×10^{-5}
N_2H^+	1–0	$J = 1–0, F_1 = 2–1, F = 3–2$	3.6×10^{-5}	4.5	67	0.11	6.0×10^{-6}
CH_3OH	2–1	$J = 2–1, K = 0 – 0$	3.4×10^{-6}	7.0	65	0.11	6.4×10^{-6}
H^{13}CN	1–0	$J = 1–0, F = 2–1$	2.2×10^{-5}	4.1	48	0.08	3.3×10^{-6}
H^{13}CO^+	1–0	$J = 1–0$	3.9×10^{-5}	4.2	25	0.04	1.8×10^{-6}
HN^{13}C	1–0	$J = 1–0, F = 2–1$	1.9×10^{-5}	4.2	—	—	—
SiO	2–1	$J = 2–1$	2.9×10^{-5}	6.3	—	—	—

Notes. The lines are sorted by decreasing value of their intensity. ^(a) Simplified transition used everywhere else in the paper. ^(b) Complete list of quantum numbers associated to the transition whose frequency is listed in Table A.1. This frequency is the one used to fix the velocity scale.

Photo-Dissociation Region (PDR) is linked to the incident far UV field, G_0 at $A_V = 0$, through

2.5. Noise properties, data size, percentage of signal channels, and line integrated intensities

$$T_d = 12.2 G_0^{0.2} \text{ K}, \quad (3)$$

where the G_0 value is given in units of the local interstellar radiation field (ISRF, Habing 1968). We invert this equation to give an approximate value of the far-UV illumination. This value is likely a lower limit to the actual G_0 in most of the mapped region. Indeed, it is the far-UV field at the surface of the PDR, while there are embedded H II regions in the FoV. However, Abergel et al. (2002) estimates a typical $G_0 \sim 100$ for the western edge of L 1630, which is a large scale edge-on PDR. Using Eq. (3), this value is compatible with the typical dust temperature fitted towards this edge, that is, approximately 30 K.

Lombardi et al. (2014) compared the obtained $850 \mu\text{m}$ opacity map to an extinction map in the K band (A_K) of the region. A linear fit of the scatter diagram of A_K and τ_{850} gives $A_K = 3460 \tau_{850}$ for Orion B (Lombardi et al. 2014, name this factor γ). They used a value of $A_K/A_V = 0.112$ from Rieke & Lebofsky (1985). However, this value, including their estimated $R_V \simeq 3.1$, is not based on observations towards Orion stars. Cardelli et al. (1989) measured the properties of dust absorption E_{B-V} and R_V towards two stars of our FoV. Using their parametrization, we yield $A_K/A_V = 0.1254$ for $R_V = 4.11$ towards HD 37903, and $A_K/A_V = 0.1335$ for $R_V = 5.30$ towards HD 38087. We here take an average of both values, $A_K/A_V = 0.13$, that is, a 20% larger value than Rieke & Lebofsky (1985). We therefore have

$$A_V = 2.7 \times 10^4 \tau_{850} \text{ mag.} \quad (4)$$

The dust properties (both the temperature and visual extinction) are measured at an angular resolution of $36''$.

The median noise levels (computed on the cubes that have 0.5 km s^{-1} channel spacing and $31''$ angular resolution) range from 100 to 180 mK (T_{mb}) depending on the observed frequency. Details can be found in Appendix A. The reduced data cube amounts to approximately 160 000 images of 325×435 pixels or 84 GB of uncompressed data. It would make a movie of 1h50m at 24 images per second. However, approximately 99.5% of the channels show mostly noise because of the limited sensitivity of our observation. The 0.5% of the bandwidth where clear signal is detected includes the emission from low J lines of CO, HCO^+ , HCN, HNC, CN, CS, SO, C_2H , c- C_3H_2 , N_2H^+ , CH_3OH , SiO, and some of their isotopologues, in particular, CO isotopologues (see Table 3 and Fig. 2).

Most of this paper studies the properties of the line integrated intensity³ defined as $W = \int T(v) dv$. To produce reliable spectral line maps, we used all the pixels matching two conditions: 1) its own signal-to-noise ratio is larger than four, and 2) the signal-to-noise ratio of at least 25% of its neighbors are larger than four. Residual striping may be seen along the vertical scanning direction, in particular at low intensity on the images of line integrated intensities. Indeed, baselining corrects for the striping to first order. Hence residual striping is more visible for faint lines and/or lines for which the overlapping of the velocity and the hyperfine structures (HCN ground state transition, for example) requires the definition of wider baselining windows. Finally, we used two different flavors of the integrated intensity. On one hand, we use the line intensity integrated over the full line profiles when we aim to study the gas properties along the full line of sight. This happens, for instance, when we compute the CO-traced mass in Sect. 3.4 and the correlations between

³ The data products associated with this paper are available at <http://www.iram.fr/~pety/ORION-B>

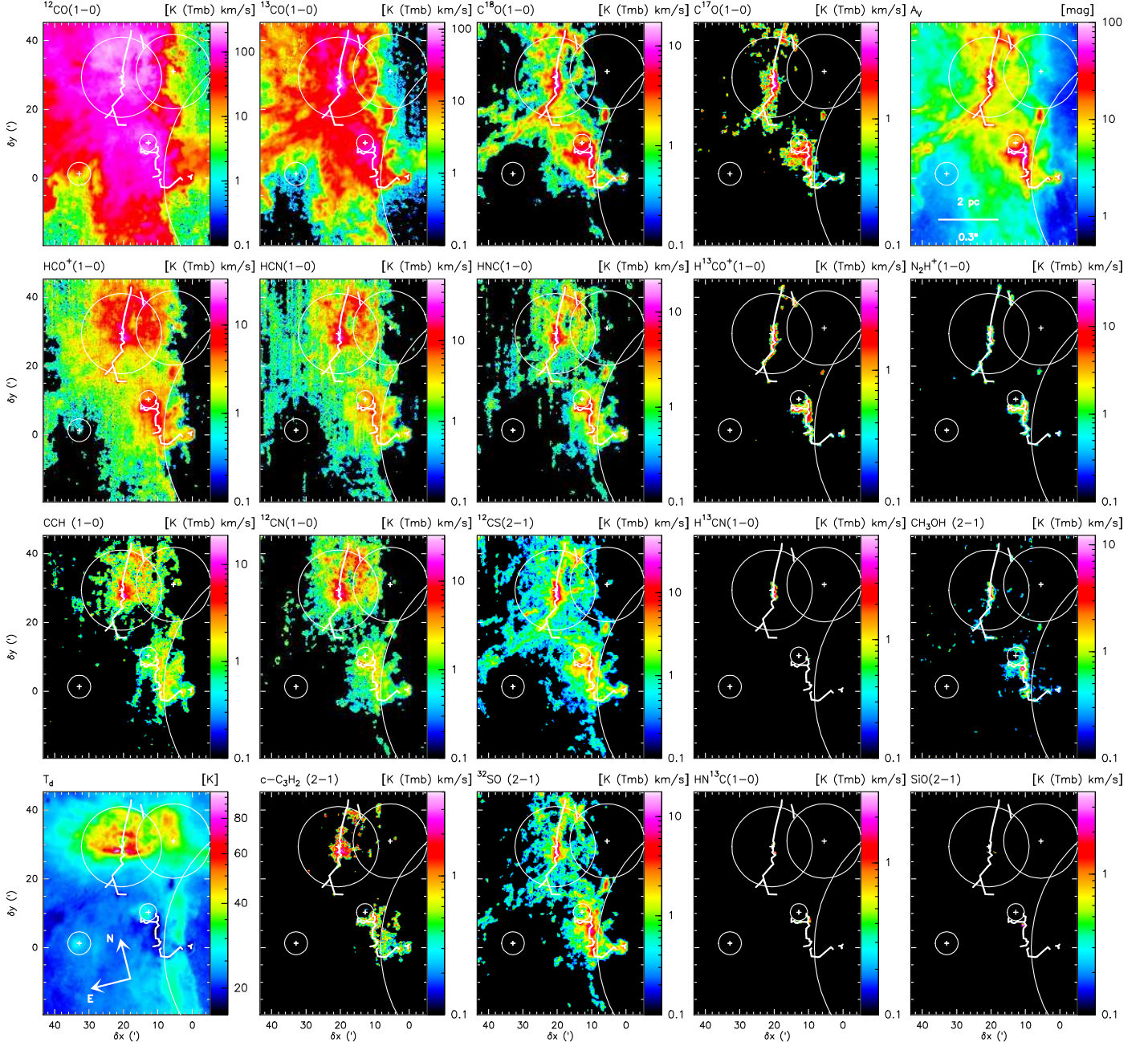


Fig. 2. Spatial distribution of the line integrated intensity for some of the detected lines in the 3 mm band, plus the dust temperature (bottom left panel) and the visual extinction (top right corner). Continuum data comes from the publicly available SED fit done by Lombardi et al. (2014) on the *Herschel* Gould Belt Survey data (PI: P. André). The color-scales are logarithmic to reveal the distribution of faint signal. Pixels with a signal-to-noise lower than four were blanked out. In addition to the circles and crosses that show the approximate boundaries of the H II regions and the associated exciting stars, we overlaid broken lines that were somewhat arbitrarily drawn by connecting the N_2H^+ (1–0) emission.

the column density of material along the full line of sight and the line integrated intensity in Sect. 5. On the other hand, lines are detected over different velocity ranges. Using the same velocity range for all lines, $[-2, +18 \text{ km s}^{-1}]$ for example, results in noisy integrated intensities for tracers that have the narrowest lines. In contrast, adapting the velocity range to each line could bias the results. We thus adopted a compromise for sections where we can restrict our investigations to the bulk of the gas: we computed the line integrated intensity over the velocity range where the core of the line can be found for each species and transition over the measured FoV. This velocity range is $[9, 12 \text{ km s}^{-1}]$.

3. Mean properties

From this section on, we only study the properties of the (1–0) line for the CO isotopologues (^{12}CO , ^{13}CO , C^{18}O , and C^{17}O), HCO^+ , HCN , HNC , and their ^{13}C isotopologues, ^{12}CN , C_2H , and N_2H^+ , as well as the (2–1) transition for ^{12}CS , ^{32}SO , CH_3OH , and SiO .

3.1. Geometry, spatial dynamic, typical visual extinction, dust temperature, and far UV illumination

Table 2 lists the typical properties of the observed FoV. At a typical distance of $\sim 400 \text{ pc}$ (Menten et al. 2007; Schlafly et al. 2014),

the mapped FoV corresponds to 5.6×7.5 pc. This corresponds to a surface of 43 pc 2 . Assuming that the depth along the line of sight is similar to the dimension projected on the plane of sky, we get a volume equal to the surface at the power 3/2, or 280 pc 3 .

The angular resolution ranges from 22.5 to $30.4''$ at 3 mm while the typical 30 m position accuracy is $\sim 2''$. All the cubes were smoothed to $31''$ angular resolution, that is, 60 mpc or $\sim 10^4$ AU. We thus explore a maximum spatial dynamic range of 125 for all the lines.

The visual extinction ranges from 0.7 to 222 mag with a mean value of 4.7 mag. This is associated to a range of ^{12}CO ($1-0$) integrated intensity from 0 to 288 K km s $^{-1}$ with a mean value of 61 K km s $^{-1}$. In other words, the FoV contains all kind of gas from diffuse, without CO emission, to highly visually extinct with bright CO emission, but most of the gas is in the higher end of the translucent regime ($2 \lesssim A_V \lesssim 6$).

The SED-fitted dust temperature along the line of sight ranges from 16 to 99 K with a mean value of 26 K. This translates into a typical far UV illumination, G_0 , ranging from 4 to 3.6×10^4 using the Inter-Stellar Radiation Field (ISRF) definition by Habing (1968). The G_0 mean value is 45 . This confirms that the observed FoV is on average strongly far-UV illuminated by the different massive exciting stars listed in Table 1 (see Sect. 2.1).

3.2. Distribution of line integrated intensities

Figure 2 presents the spatial distribution of the line integrated intensities. We also included the spatial distribution of the dust temperature in the bottom left panel and the visual extinction in the top right panel to give reference points on the underlying nature of the gas that emits each line tracer (see Sect. 2.4).

The spatial distributions of the molecular lines presented here are different. The ($1-0$) line of the CO isotopologues themselves show a very different behavior. The line of the rarer isotopologue, C^{17}O , has a spatial distribution that is similar to that of the N_2H^+ ($1-0$) line, which is a known tracer of the cold and dense regions in molecular clouds (Bergin & Tafalla 2007). Indeed, N_2H^+ and C^{17}O are seen only towards lines of sight of high extinction ($A_V > 20-30$). The ($1-0$) line emission of the slightly more abundant isotopologue C^{18}O is more extended and clearly traces the dense and cold filaments of the cloud. Moreover, the C^{18}O ($1-0$) emission is similar to the extinction map shown in Fig. 2, a property consistent with the known linear correlation of C^{18}O ($1-0$) integrated intensity with the visual extinction (Frerking et al. 1982). The ($1-0$) emission of the second most abundant CO isotopologue, ^{13}CO , traces gas in the extended envelope surrounding the filaments traced by the C^{18}O ($1-0$) emission. The emission of the main CO isotopologue no longer traces the dense gas and is largely dominated by the extended and more diffuse or translucent gas because it is then strongly saturated.

The HCO^+ , HCN, and HNC ($1-0$) lines are usually considered to be good tracers of dense molecular gas because of their high spontaneous emission rates and large critical densities. Among these three species, the HNC ($1-0$) map bears the closest resemblance to the C^{18}O ($1-0$) map. Emission in the ground state lines of HCO^+ and HCN exhibits a more extended component and more closely resembles the ^{13}CO ($1-0$) map. All three lines as well as CN, present bright emission towards high-extinction lines of sight. Their emission also seems to trace the edges of the H II regions. A clear difference between CN and the

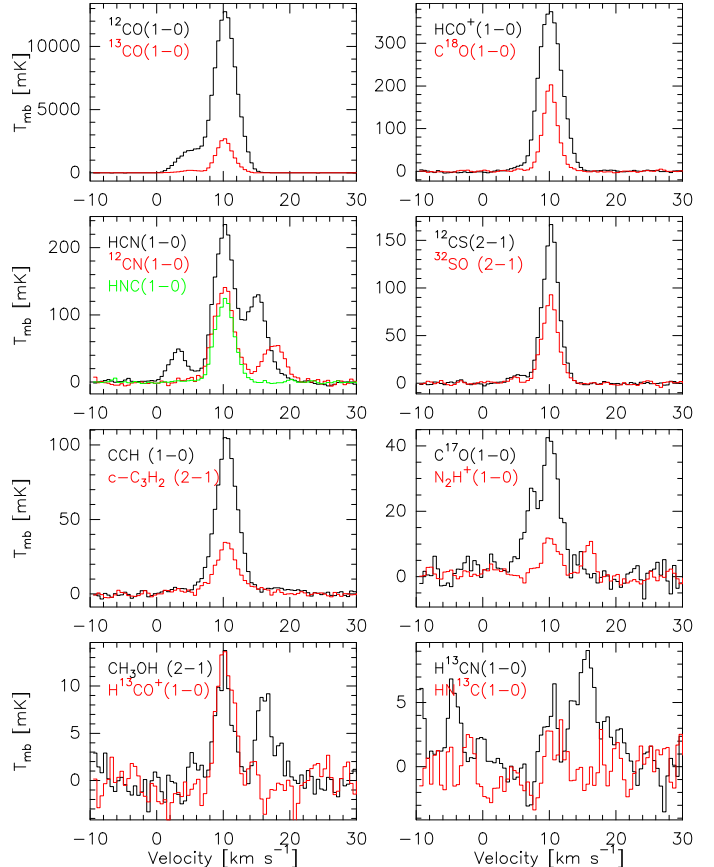


Fig. 3. Spectra averaged over the mapped field of view.

other N -bearing species and HCO^+ is the larger contrast between the warmer northern region, near NGC 2024, and the cooler southern region near the Horsehead. In contrast to their main isotopologue, the ^{13}C isotopologues of HCO^+ , HCN, and HNC are only clearly detected towards the dense cores. The methanol emission is slightly more extended than the N_2H^+ ($1-0$) emission but it is clearly seeded by the dense cores as traced by N_2H^+ .

The emission of the sulfur-bearing species, in particular the ^{12}CS ($2-1$) line, has similar spatial distributions to that of the C^{18}O ($1-0$) line. Finally, the SiO ($2-1$) line is only detected at the position of two previously known outflows. The first is located at the south-west of NGC 2023 around the class-0 NGC 2023 mm1 protostars located at $05^{\text{h}}41^{\text{m}}24.9^{\text{s}}, -02^{\circ}18'09''$ (J2000, Sandell et al. 1999), while the second is located on both sides of the FIR5 young stellar object located at $05^{\text{h}}41^{\text{m}}44.6^{\text{s}}, -01^{\circ}55'38''$ (J2000, Richer 1990; Chernin 1996), near the center of NGC 2024. This confirms that SiO is, above all, a shock tracer.

3.3. Mean line profiles over the observed FoV

Figure 3 shows the spectra of the main detected lines averaged over the mapped FoV. Several spectra show multiple components for different reasons. First, the multi-peak nature of the CN, HCN, C^{17}O and N_2H^+ ground state lines is a consequence of the resolved hyperfine structure of these transitions. Second, the faintest spectra (e.g., HN^{13}C) are detected at low signal-to-noise ratio, implying a noisy profile. Finally, the western side of the Orion B cloud displays two velocity components: the main one at approximately 10.3 km s $^{-1}$ and a satellite one, ten times fainter, at approximately 4.9 km s $^{-1}$. The two components have

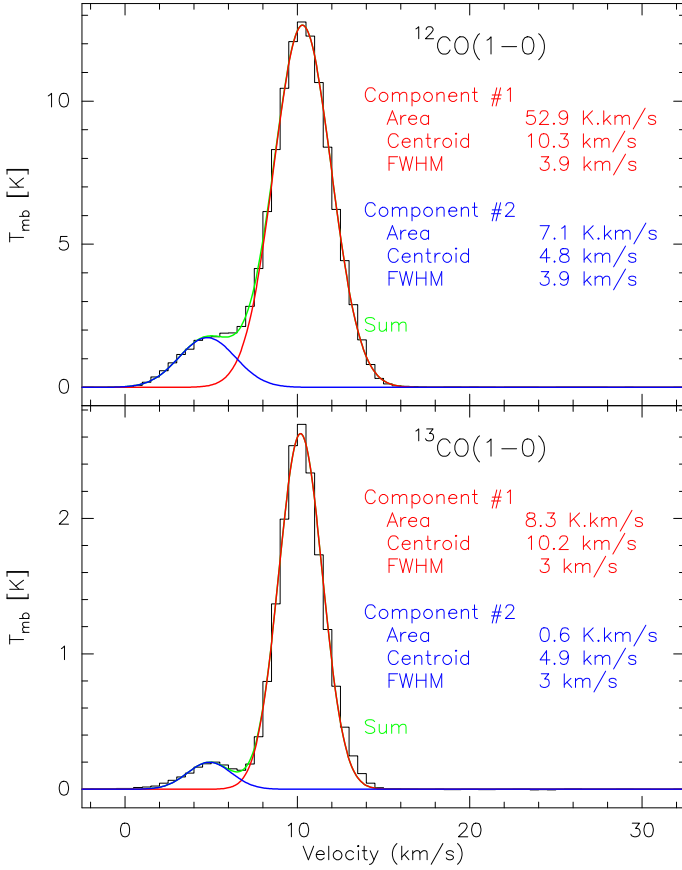


Fig. 4. Gaussian fits of the two main velocity components that appear in the western edge of Orion B.

similar line width ($3\text{--}4 \text{ km s}^{-1}$) and they overlap between 5 and 9.5 km s^{-1} . Figure 4 displays the fit for these two components on the ^{12}CO and ^{13}CO ($1-0$) spectra averaged over the FoV. The values of the $^{12}\text{CO}/^{13}\text{CO}$ integrated line intensity ratios are 6.4 and 11.8 for the main and the satellite components, respectively. The difference in line ratios suggests that the satellite velocity component corresponds to lower column density material (see Sect. 6.1). The satellite component is barely detected in C^{18}O , HCO^+ , and ^{12}CS , and remains undetected for the other lines. Figure 5 shows the ^{12}CO ($1-0$) emission in two channel maps belonging to the two velocity components, both in linear and logarithmic color scales. The use of a logarithmic transfer function shows that bright emission is surrounded by a halo of faint emission. This shows that the fainter velocity component still covers a large fraction of the observed surface.

We now argue that both velocity components along the line of sight are associated with the Orion B GMC. Figure 5 shows that the spatial distribution of both components overlap on most of the observed field, and that they are in close interaction with the massive stars of known distance listed in Table 1. Furthermore, the 3D structure of interstellar extinction has been studied by Lallement et al. (2014) and Green et al. (2015) using differential reddening of stars at known distances. Towards Orion B, the reddening steeply increases between 300 and 500 pc, and most importantly, there is no significant reddening detected at closer or larger distances in this direction of the sky (Lallement, priv. comm.). These results are in excellent agreement with the distance determination of Orion through maser parallax (Menten et al. 2007). Overall the 3D structure of the Orion clouds is complex and could extend over several tens of parsec

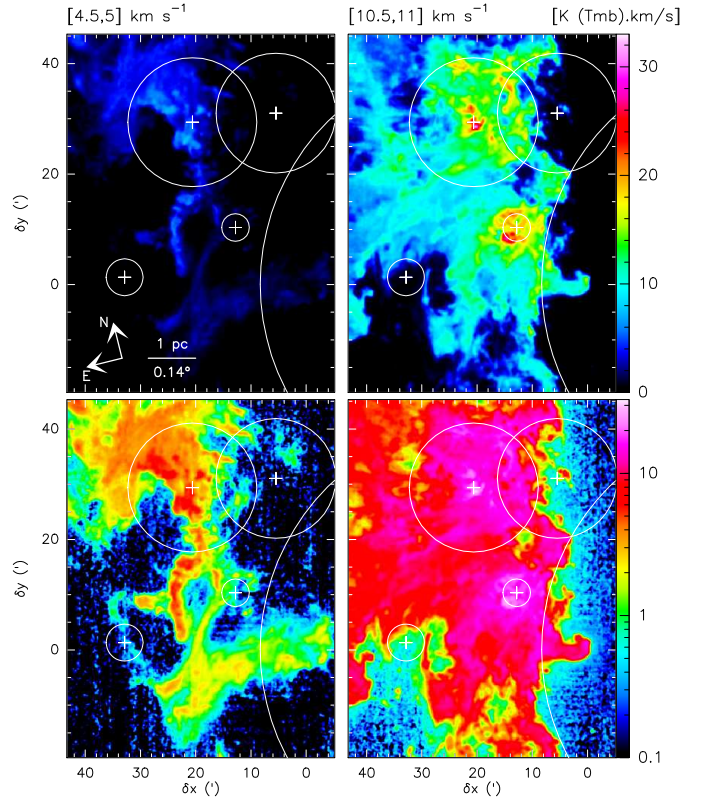


Fig. 5. Spatial distribution of the ^{12}CO ($1-0$) emission integrated over two different 0.5 km s^{-1} velocity ranges on linear (top row) and logarithmic (bottom row) color scales.

along the line of sight, a dimension comparable to the projected size on the plane of the sky.

Table 3 lists the integrated line intensities, W , and luminosities, L , computed as

$$\frac{L}{L_{\odot}} = 3.4 \times 10^{-8} \left(\frac{3 \text{ mm}}{\lambda} \right)^3 \left(\frac{W}{1 \text{ K km s}^{-1}} \right) \left(\frac{D}{400 \text{ pc}} \right) \left(\frac{\Omega}{1' \times 1'} \right),$$

where k_{bolt} is Boltzmann constant, λ is the line rest wavelength, D is the source distance, and Ω is the FoV angle. The dynamic range of reliable integrated intensity is approximately 2400. Moreover, the typical intensity ratios of the ($1-0$) lines would be $^{12}\text{CO}/^{13}\text{CO} = 6.7$, $^{13}\text{CO}/\text{C}^{18}\text{O} = 16.7$, $\text{C}^{18}\text{O}/^{12}\text{CO} = 0.9\%$, and $\text{HCO}^+/\text{HCN}/^{12}\text{CO} \sim 3\%$. ^{12}CN , C^{18}O , ^{12}CS , C_2H , and HNC emit approximately 1% of the ^{12}CO intensity. The low- J lines of ^{32}SO , C^{17}O , $\text{c-C}_3\text{H}_2$, N_2H^+ , H^{13}CN , H^{13}CO^+ are up to 25 times fainter than the previous family, exemplified by C^{18}O . The HN^{13}C and SiO integrated intensity can not be reliably measured.

3.4. CO-traced, dust-traced, and virial-traced mass and densities

In this section, we compute the typical gas mass and densities using three common approaches: 1) the ^{12}CO ($1-0$) luminosity, 2) the dust continuum luminosity, and 3) the virial theorem. Table 2 lists the found values.

The direct sum of the pixel intensity over the mapped FoV and between the $[-2, +18] \text{ km s}^{-1}$ velocity range indicates that the data cube contains a total CO luminosity of $\sim 2500 \text{ K km s}^{-1} \text{ pc}^2$. Using the standard CO-to-H₂ conversion factor, $X_{\text{CO}} = 2.0 \times 10^{20} \text{ cm}^{-2}/(\text{K km s}^{-1})$ or

$4.35 M_{\odot} \text{ pc}^{-2}/(\text{K km s}^{-1})$ (this includes the factor 1.36 to account for the presence of helium, Bolatto et al. 2013), this corresponds to a gas mass of $1.1 \times 10^4 M_{\odot}$. The total surface covered was 0.86 square degrees, that is, 43 pc^2 . The mean intensity and mean surface density are 61 K km s^{-1} and $260 M_{\odot} \text{ pc}^{-2}$, respectively. The associated column density of gas is approximately $10^{22} \text{ H}_2 \text{ cm}^{-2}$. This in turn gives a typical volume density of $40 M_{\odot} \text{ pc}^{-3}$ or $590 \text{ H}_2 \text{ cm}^{-3}$.

Using the Gould Belt Survey data and its SED fits, we can derive values for the same quantities from dust far infrared emission. To do this, in Sect. 2.4 we first used a value different from the standard one for the conversion factor from A_K to A_V because 1) this is an observational quantity that can be measured relatively easily, and 2) we mainly deal with molecular gas, while the standard value is derived in diffuse gas. While this value depends on the optical properties (grain composition, grain shapes, and size distribution, which leads to the extinction curve) of the dust in Orion B, it is independent of any assumption about the gas properties. On the other hand, to derive the dust traced mass, we also need to use a value for the N_{H}/A_V ratio. Assuming that the dependency of this ratio on the dust optical properties is only a second order effect, this ratio mainly depends on the gas-to-dust ratio, that is, on how many grains there are per unit mass of gas. We thus use the standard value, $N_{\text{H}}/A_V = 1.8 \times 10^{21} \text{ H cm}^{-2} \text{ mag}^{-1}$, for this ratio. This directly leads to a dust-traced mass of the mapped FoV of $\sim 3900 M_{\odot}$, a mean surface density of $92 M_{\odot} \text{ pc}^{-2}$ or $4 \times 10^{21} \text{ H}_2 \text{ cm}^{-2}$, and a mean volume density of $14 M_{\odot} \text{ pc}^{-3}$ or $210 \text{ H}_2 \text{ cm}^{-3}$.

The column density of neutral atomic hydrogen measured by integrating across profiles of the 21 cm H I line taken by the LAB all-sky H I survey (Kalberla et al. 2005) is

$$N(\text{H I}) = 1.823 \times 10^{18} \text{ cm}^{-2} \int T_B dv \approx (1.8 \pm 0.2) \times 10^{21} \text{ cm}^{-2}, \quad (5)$$

in the optically thin limit. This corresponds to approximately 1.0 mag of visual extinction using the usual conversion $N_{\text{H}}/E_{B-V} = 5.8 \times 10^{21} \text{ cm}^{-2} \text{ mag}^{-1}$ derived by Bohlin et al. (1978) and $R_V = E_{B-V}/A_V = 3.1$. The total expected foreground gas contribution for a source at a distance of 400 pc is $N_{\text{H}} = 1.2 \times 10^{21} \text{ cm}^{-2}$ for a local mean gas density $\langle n(\text{H}) \rangle = 1.15 \text{ cm}^{-3}$ (Spitzer 1978) corresponding to $A_V = 0.75 \text{ mag}$ using the same conversion from column density to extinction. The minimum value of the visual extinction across the observed FoV, (i.e., 0.7) is therefore in good agreement with the expected contribution of diffuse material along the line of sight. As the mean visual extinction is 4.7 mag, correcting for this diffuse component would result in decreasing the molecular part of the dust-traced mass and densities by less than 20%. We choose to consider this difference negligible, that is, to consider that all the dust-traced mass refers to gas where hydrogen is molecular.

Following Solomon et al. (1987) and Bolatto et al. (2013), we can also compute a mass assuming that turbulent pressure and gravity are in virial equilibrium. Bolatto et al. (2013) indicate that the virial mass, M_{vir} , is given by

$$M_{\text{vir}} = f R \sigma^2, \quad (6)$$

where R is the projected radius of the measured FoV, σ is the 1D velocity dispersion (full width at half maximum of a Gaussian divided by 2.35), and f is a factor that takes into account projection effects. This factor depends on the assumed density profile of the GMC. For a spherical volume density distribution with a power-law index k , that is,

$$\rho(r) \propto r^{-k}, \quad (7)$$

f is 1160, 1040, and $700 M_{\odot} \text{ pc}^{-1} (\text{km s}^{-1})^{-2}$, for $k = 0, 1$, and 2, respectively. In our case, $R \approx 0.5 \sqrt{5.6 \times 7.5} = 3.3$, and $\sigma \approx 3.9/2.35 = 1.7 \text{ km s}^{-1}$, when we only take into account the Gaussian fit of the main velocity component at approximately 10.5 km s^{-1} . We thus obtain a virial mass between 6200 and $9500 M_{\odot}$.

We find that, contrary to expectations, the CO-traced mass is typically three times the dust-traced mass, and that the virial mass is lower than the CO-traced mass but is much higher than the dust-traced mass. Throughout the paper, we propose that this discrepancy is related to the strong far-UV illumination of the mapped FoV (see Sect. 3.1). In the meantime, we will take an average between the CO-traced and dust-traced mass and densities when we require an order of magnitude estimate for these quantities.

4. Fraction of line fluxes from different gas regimes

In this section, we explore which fraction of the line fluxes comes from more or less dense gas, and from more or less far-UV illuminated gas.

4.1. Flux profiles over different A_V ranges

We chose four ranges of A_V , representing diffuse ($1 \leq A_V < 2$), and translucent ($2 \leq A_V < 6$) gas, the environment of filaments ($6 \leq A_V < 15$), and dense gas ($15 \leq A_V$). Table 4 lists the physical properties of the different regions based on their ^{12}CO (1–0) and far infrared emission. While the different regions have, by construction, increasing values of their mean visual extinction (1.4, 4, 9, and 29, respectively), they present similar mean dust temperature and far UV illumination. As expected the minimum dust temperature decreases when the range of visual extinction increases. In contrast, the maximum dust temperatures, and thus far UV illuminations, are also found in the masks of highest visual extinctions. This is related to the presence of very dense (probably cold) molecular gas in front of young massive stars that excite H II regions (see, e.g., the dark filament in front of IRS2 that excites the NGC 2024 nebula). This could also be due to the presence of embedded heating sources.

Contrary to standard expectations, the dust and CO-traced mass are similar for diffuse and dense regions, while they differ by a factor three, mostly in the translucent gas and filament environment. Moreover, both the dust and CO-traced matter indicate that approximately 50% of the gas lies in diffuse and translucent gas. Dense cores ($15 \leq A_V$) represent between 10 and 20% of the mass but only 3% of the surface and 0.6% of the volume. The sum of the volume fractions of the four regions only amounts to 55% because of the simplified way the volumes are computed ($V = S^{3/2}$). This implies that volume densities can only be interpreted as typical values. Finally, the volume densities increase from ~ 100 to $7300 \text{ H}_2 \text{ cm}^{-3}$ for diffuse and dense gas, respectively. Translucent gas and the environment of filaments have typical density values of ~ 500 and $1500 \text{ H}_2 \text{ cm}^{-3}$, respectively. The volume density increases by a factor of between three and five from one gas regime to the next. We will use this fact to statistically identify high/low A_V lines of sight with high/low density gas, respectively.

Figure 6 presents the A_V masks and displays flux profiles integrated over regions of different extinction ranges. To better quantify the different behavior of the fluxes integrated over these different regions, Table 5 and Fig. 7 present, for each line, the percentage of the total line flux that comes from the different A_V

Table 4. Properties of the A_V masks sorted by increasing range of visual extinction.

Parameter	Unit	$1 \leq A_V < 2$	$2 \leq A_V < 6$	$6 \leq A_V < 15$	$15 \leq A_V < 222$
$W_{\text{CO}}^{\min} - W_{\text{CO}}^{\text{mean}} - W_{\text{CO}}^{\max}$	K km s^{-1}	0–6.8–46.9	1.3–62.6–211	24.8–122–261	41.5–137–288
$A_V^{\min} - A_V^{\text{mean}} - A_V^{\max}$	mag	1–1.4–2	2–3.6–6	6–8.5–15	15–28.9–222
$T_d^{\min} - T_d^{\text{mean}} - T_d^{\max}$	K	19–24–45	19–26–67	18–29–99	16–26–95
$G_0^{\min} - G_0^{\text{mean}} - G_0^{\max}$	ISRF (Habing 1968)	8.9–30–680	8.4–46–5100	6–72–36 000	4–47–28 000
CO-traced mass	M_{\odot}	320 (3%)	5600 (51%)	4400 (40%)	830 (8%)
Dust-traced mass	M_{\odot}	300 (8%)	1500 (38%)	1400 (36%)	790 (20%)
Emitting surface	pc^2	11 (25%)	21 (48%)	8.4 (20%)	1.4 (3.3%)
Typical volume	pc^3	36 (13%)	93 (33%)	24 (8.6%)	1.7 (0.6%)
CO-traced mean column density	$M_{\odot} \text{ pc}^{-2} 10^{21} \text{ H}_2 \text{ cm}^{-2}$	30 1.4	270 12	530 24	590 27
Dust-traced mean column density	$M_{\odot} \text{ pc}^{-2} 10^{21} \text{ H}_2 \text{ cm}^{-2}$	28 1.3	71 3.3	160 7.6	560 26
CO-traced mean volume density	$M_{\odot} \text{ pc}^{-3} \text{H}_2 \text{ cm}^{-3}$	8.9 130	60 890	180 2700	500 7500
Dust-traced mean volume density	$M_{\odot} \text{ pc}^{-3} \text{H}_2 \text{ cm}^{-3}$	8.4 130	16 230	57 850	470 7100

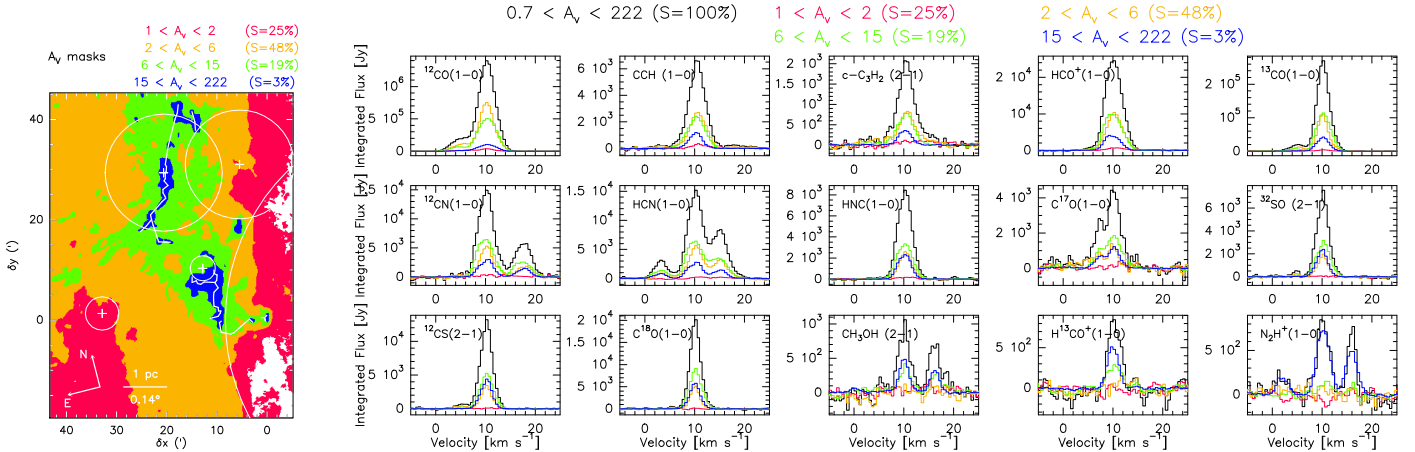


Fig. 6. Left: spatial distribution of the four following masks: $1 \leq A_V < 2$ in red, $2 \leq A_V < 6$ in orange, $6 \leq A_V < 15$ in green, and $15 \leq A_V < 222$ in blue. The percentages in the legend list the fraction of the surface contained in the different masks. Right: flux is integrated over the masks as a function of velocity. The spectrum of different colors shows the evolution of the flux in each line as a function of the mask used: all pixels observed in black, all pixels with $1 \leq A_V < 2$ in red, $2 \leq A_V < 6$ in orange, $6 \leq A_V < 15$ in green, and $15 \leq A_V < 222$ in blue.

masked regions (F_{A_V}/F_{tot}). In all cases, the fluxes are integrated in the [9, 12 km s $^{-1}$] velocity range. The lines were sorted by decreasing value of the sum of $F(1 \leq A_V < 2)$ and $F(2 \leq A_V < 6)$. This value represents the flux coming from both diffuse and translucent gas for each line. The layout of the panels in Fig. 6 also follows this order. We can group the lines into four categories depending on how the line flux is divided between regions of very low ($1 \leq A_V < 2$), low ($2 \leq A_V < 6$), intermediate ($6 \leq A_V < 15$), or high ($15 \leq A_V$) visual extinction.

In the first category of lines, the regions of low and intermediate visual extinctions contribute more than $\sim 45\%$ of the total flux, and regions of high visual extinction contribute less than $\sim 20\%$ of the flux. In this category, the total flux is predominantly coming from translucent lines of sight ($2 \leq A_V < 6$). This is the case of the (1–0) lines of ^{12}CO , HCO^+ , C_2H , and the $\text{c-C}_3\text{H}_2$ (2–1) line. From these species, ^{12}CO is the one with the largest contribution (55%) from diffuse and translucent gas ($A_V \leq 6$).

In the 2nd category, the total flux is now predominantly coming from regions of intermediate visual extinction (45% coming from $6 \leq A_V < 15$), but the diffuse and translucent gas still contributes a similar fraction (35–40%) of the total flux, and dense gas does not contribute more than 20% of the total flux. This is the case of the (1–0) lines of ^{13}CO , HCN , and CN .

In the third category, the flux comes predominantly from regions of intermediate visual extinction as in the 2nd category, but the regions of low and high visual extinctions both contribute similar fractions of the total flux (approximately 30%). The (1–0) lines of HNC , C^{18}O , C^{17}O , and the lines of the sulfur species, namely the (2–1) line of ^{12}CS , and ^{32}SO , belong to this category.

The (1–0) lines of N_2H^+ and H^{13}CO^+ , as well as the (2–1) lines of CH_3OH form the last category. In this one, the flux is predominantly coming from the regions of high visual extinction ($15 \leq A_V$). These lines all present a small surface filling factor ($\lesssim 5\%$) and negligible contribution from the translucent and diffuse gas. In this category, N_2H^+ plays a special role. This is the only easily mapped line, where the flux is completely dominated (at 88%) by regions of high visual extinction; probably dense cores.

4.2. Flux profiles over different T_d ranges

We chose four ranges of T_d , representing cold dust ($16 \leq T_d < 19.5$ K) that corresponds to gas that is shielded from the UV field (e.g., the dense cores), lukewarm dust ($19.5 \leq T_d < 23.5$ K), warm dust ($23.5 \leq T_d < 32$ K), and hot dust ($32 \leq T_d < 100$ K). It is clear that this fitted dust temperature is biased toward the

Table 5. Percentage of the total line fluxes inside the four A_V mask regions, integrated over $[9, 12 \text{ km s}^{-1}]$.

Species	Transition	$0 \leq A_V < 222$	$1 \leq A_V < 2$	$2 \leq A_V < 6$	$6 \leq A_V < 15$	$15 \leq A_V < 222$
^{12}CO	1–0	100%	2.5%	52%	38%	7.6%
C_2H	1–0	100%	4.4%	41%	37%	17%
c- C_3H_2	2–1	100%	4.5%	40%	38%	17%
HCO^+	1–0	100%	2.8%	41%	40%	16%
^{13}CO	1–0	100%	1.4%	38%	45%	15%
HCN	1–0	100%	1.7%	36%	44%	18%
^{12}CN	1–0	100%	2.6%	33%	45%	19%
HNC	1–0	100%	2.1%	29%	41%	27%
C^{17}O	1–0	100%	5.6%	25%	43%	26%
^{12}CS	2–1	100%	0.68%	25%	42%	32%
^{32}SO	2–1	100%	0.86%	24%	44%	31%
C^{18}O	1–0	100%	0.49%	23%	48%	29%
CH_3OH	2–1	99%	4.4%	5.8%	41%	48%
H^{13}CO^+	1–0	98%	0.67%	7.1%	34%	56%
N_2H^+	1–0	100%	-11%	8.2%	17%	88%

Notes. The lines are sorted by decreasing value of the flux coming from the diffuse and translucent lines of sight.

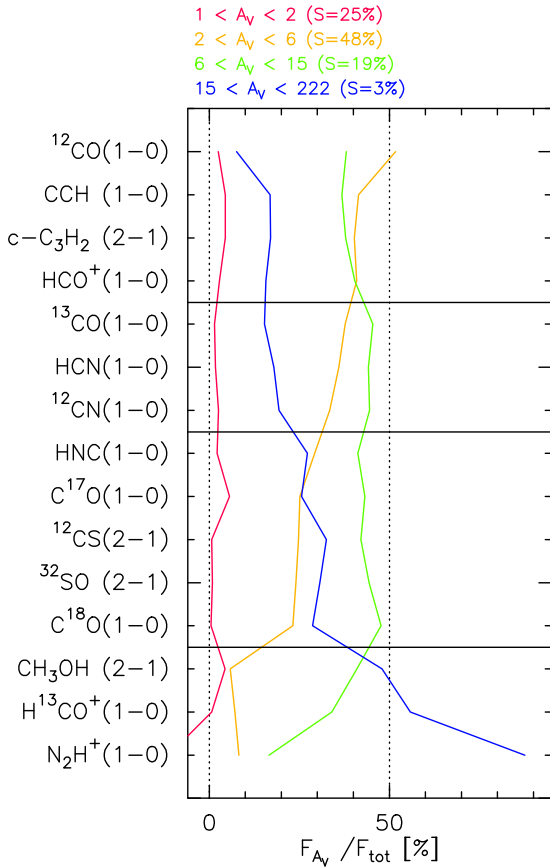


Fig. 7. For each line, flux integrated over each of the four A_V masks divided by the flux computed over the observed field of view. All fluxes are computed between 9 and 12 km s^{-1} . The black horizontal lines define the groups of lines described in Sect. 4.1.

presence of warm dust because the dust emissivity increases rapidly with temperature in the far infrared. Hence, cool dense gas is probably present along the line of sight of highest extinction, even though the fitted dust temperature is relatively high.

Here we use the dust temperature as a proxy for the typical far-UV illumination along the line of sight (see Sect. 2.4). In fact, using Eq. (3), we obtain a mean far-UV illumination of $9, 18, 50$, and 400 for the cold, lukewarm, warm, and hot dust masks, respectively. This implies very different kinds of PDRs present along the line of sight. Moreover, the four masks of dust temperature display a morphology very different from that of the masks of visual extinction. Only the dense cores in Horsehead and near NGC 2023 are clearly delineated in both families of masks, while the intermediate density filamentary structure and diffuse/translucent gas are present in all four masks of dust temperature. Instead, the morphology of these temperature masks coincides well with the boundaries of the different H II regions. We thus interpret the cold, lukewarm, warm, and hot dust masks as very low, low, medium, and high far-UV illumination masks.

The FoV is dominated by intermediate far-UV illumination PDRs (83% of the surface have a G_0 between 10 and 120). Less than 2% of the lines of sight have $G_0 \leq 10$ and approximately 15% have $G_0 > 120$. Moreover, the CO-traced mass is 0.86, 2.6, 3.1, and 3.5 times the dust-traced mass in the cold, lukewarm, warm, and hot dust regions, respectively. Similar ratios are found for the volume densities. This confirms that the discrepancy between CO and dust traced mass is linked to the enhanced far-UV illumination of the south-western edge of Orion B.

Figure 8 presents the T_d masks and displays the flux profiles integrated over regions of different far-UV illumination. To better quantify the different behavior of the fluxes integrated over these different regions, Table 7 and Fig. 9 presents, for each line, the percentage of the total line flux that comes from the different T_d masked regions (F_{T_d}/F_{tot}). In all cases, the fluxes are integrated in the $[9, 12 \text{ km s}^{-1}]$ velocity range. The lines were sorted by decreasing distance between the sum of the flux coming from the highest far-UV illumination regions (red and orange masks) and the sum of the flux coming from the lowest far-UV illumination regions (green and blue masks). The layout of the panels in Fig. 8 also follows this order. While oscillations on the four individual curves of Fig. 9 are present, the general tendency is that the percentage of flux coming from the highest far-UV illuminated regions decreases from top to bottom. We can thus group the lines into four categories depending on whether the line flux

Table 6. Properties of the T_d masks sorted by increasing range of dust temperature.

Parameter	Unit	$16 \leq T_d < 19.5$	$19.5 \leq T_d < 23.5$	$23.5 \leq T_d < 32$	$32 \leq T_d < 100$
$W_{CO}^{\min} - W_{CO}^{\text{mean}} - W_{CO}^{\max}$	K km s^{-1}	0.2–63.8–149	0–46.5–197	0–57.4–273	0.2–114–288
$A_V^{\min} - A_V^{\text{mean}} - A_V^{\max}$	mag	1.1–17.2–127	0.7–4–69	0.8–4.1–222	0.8–7.2–186
$T_d^{\min} - T_d^{\text{mean}} - T_d^{\max}$	K	16–19–20	20–22–24	24–27–32	32–40–99
$G_0^{\min} - G_0^{\text{mean}} - G_0^{\max}$	ISRF (Habing 1968)	4–8.6–10	10–18–26	26–50–120	120–400–36 000
CO-traced mass	M_\odot	220 (2%)	3900 (35%)	4300 (39%)	2700 (25%)
Dust-traced mass	M_\odot	260 (7%)	1500 (38%)	1400 (36%)	770 (20%)
Emitting surface	pc^2	0.8 (1.8%)	19 (45%)	18 (41%)	5.5 (13%)
Typical volume	pc^3	0.7 (0.3%)	84 (30%)	73 (26%)	13 (4.6%)
CO-traced mean column density	$M_\odot \text{ pc}^{-2} \text{H}_2 \text{ cm}^{-2}$	280 13	200 9.3	250 12	490 23
Dust-traced mean column density	$M_\odot \text{ pc}^{-2} \text{H}_2 \text{ cm}^{-2}$	330 16	78 3.6	81 3.7	140 6.4
CO-traced mean volume density	$M_\odot \text{ pc}^{-3} \text{H}_2 \text{ cm}^{-3}$	310 4600	46 690	59 890	210 3100
Dust-traced mean volume density	$M_\odot \text{ pc}^{-3} \text{H}_2 \text{ cm}^{-3}$	380 5600	18 270	19 290	59 890

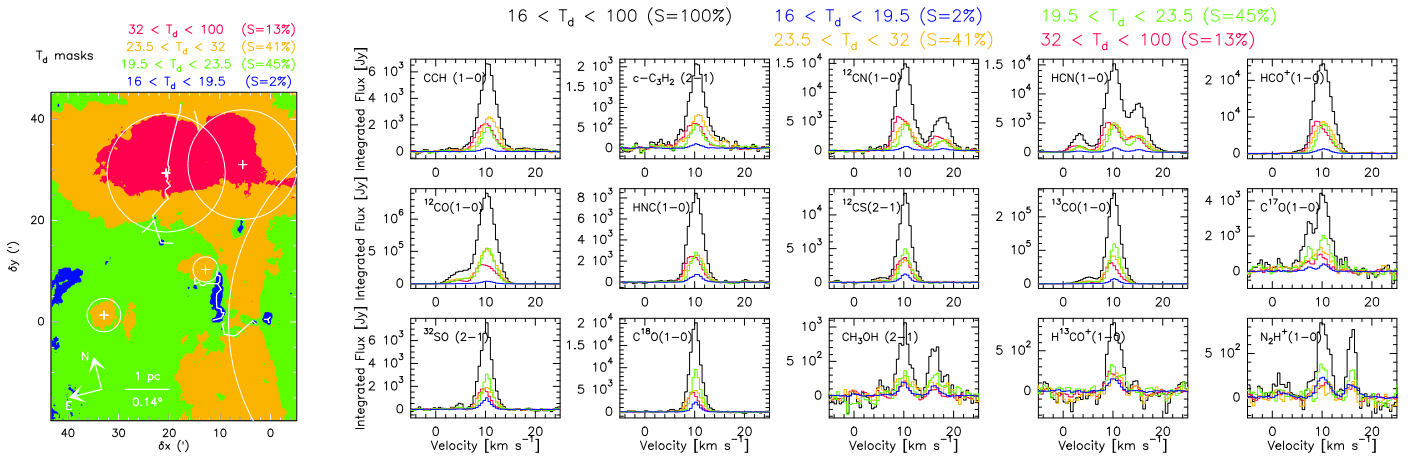


Fig. 8. *Left:* spatial distribution of the four following masks: $16 \leq T_d < 19.5$ K in blue, $19.5 \leq T_d < 23.5$ K in green, $23.5 \leq T_d < 32$ K in orange, and $32 \leq T_d < 100$ K in red. The percentages in the legend list the fraction of the surface contained in the different masks. *Right:* flux integrated over the masks as a function of velocity. The spectrum of different colors illustrates the evolution of the flux for the same line as a function of the mask used: all pixels observed in black, all pixels with $16 \leq T_d < 19.5$ K in blue, all pixels with $19.5 \leq T_d < 23.5$ K in green, all pixels with $23.5 \leq T_d < 32$ K in orange, and all pixels with $32 \leq T_d < 100$ K in red.

comes predominantly from the very low, low, medium, or high far-UV illumination regions.

In the first category, the regions of high far-UV illumination ($G_0 > 27$) contribute approximately 70% of the total line flux and the region of very low illumination ($G_0 < 10$) contributes less than 5%. High ($G_0 > 120$) and medium ($27 < G_0 < 120$) illumination regions contribute approximately equally to the total flux. The fundamental lines of the C₂H, c-C₃H₂, ¹²CN, and HCN belong to this category.

In the second category, containing the HCO⁺, HNC and ¹²CO (1–0) lines, the line flux comes predominantly (65–75%) from intermediate far UV illumination regions ($10 < G_0 < 120$). The highest illumination region still contributes 20–30% of the total flux, while the lowest illumination region contributes less than 10%.

In the third category, the flux mostly comes from the region where $10 < G_0 < 27$. Quantitatively, this is the category where the flux coming from $G_0 < 27$ starts to dominate compared to medium and intermediate illumination regions. The (1–0) line of ¹³CO and H¹³CO⁺, as well as the (2–1) line of ¹²CS, and ³²SO belong to this category.

In the last category, the flux coming from regions where $G_0 < 27$ contributes between 52 and 66% of the total flux. This contains the CH₃OH (2–1), and the (1–0) line of the rarest CO isotopologues and N₂H⁺.

5. Molecular low- J lines as a probe of the column density

5.1. Visual extinction vs. line integrated intensities

Figure 10 presents the joint distributions of the visual extinction and line integrated intensities for the studied molecular tracers. As the visual extinction is proportional to the amount of matter along the line of sight, it is desirable to make a comparison of all the matter traced by the molecules along this line of sight. Hence, the line profiles are integrated over the full velocity range where the line is measured, that is, not just integrated anymore on the [9, 12 km s⁻¹] velocity range. The visual extinctions are defined over the full FoV. In contrast, the line integrated intensities are well defined for only a fraction of the FoV. The joint distributions were thus only computed where the line integrated intensities are well defined (the criteria can be found in Sect. 2.5). For each distribution, the additional statistics (in particular for the visual extinction) are computed on this fraction of points. Table 8 lists these statistics.

The first obvious trend in Fig. 10 is the global correlation between the visual extinction, A_V , and the line integrated intensities, W . This correlation is clearly visualized through the comparison of the black curves, which show the typical behavior of the variations of A_V as a function of W , with the white lines

Table 7. Percentage of the total line fluxes inside the four T_d mask regions, integrated over [9, 12 km s $^{-1}$].

Species	Transition	$16 \leq T_d < 100$	$16 \leq T_d < 19.5$	$19.5 \leq T_d < 23.5$	$23.5 \leq T_d < 32$	$32 \leq T_d < 100$
C ₂ H	1–0	100%	3.2%	25%	39%	32%
c-C ₃ H ₂	2–1	100%	4.2%	25%	39%	31%
¹² CN	1–0	100%	4%	27%	33%	36%
HCN	1–0	100%	4.2%	29%	34%	32%
HCO ⁺	1–0	100%	4.6%	30%	36%	29%
HNC	1–0	100%	7.9%	31%	32%	29%
¹² CO	1–0	100%	2.4%	38%	38%	22%
¹² CS	2–1	100%	8.4%	35%	28%	29%
¹³ CO	1–0	100%	4.6%	41%	33%	21%
³² SO	2–1	100%	11%	38%	28%	23%
H ¹³ CO ⁺	1–0	100%	16%	33%	24%	26%
C ¹⁷ O	1–0	100%	7.9%	44%	29%	19%
CH ₃ OH	2–1	100%	18%	35%	29%	18%
C ¹⁸ O	1–0	100%	9.1%	44%	27%	20%
N ₂ H ⁺	1–0	100%	27%	39%	15%	20%

Notes. The lines are sorted by decreasing value of the flux coming from the warm and hot dust lines of sight.

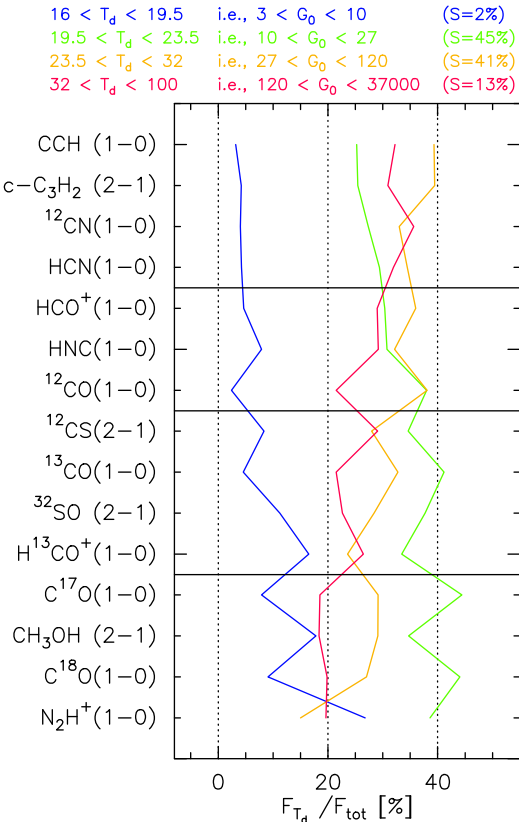


Fig. 9. For each line, flux integrated over each of the four T_d masks divided by the flux integrated over the observed field of view. All fluxes are computed between 9 and 12 km s $^{-1}$. The black horizontal lines define the groups of lines described in Sect. 4.2.

that represent a linear relationship between these two quantities. While the lines are often overly bright with respect to the white line at low extinction, and their integrated intensity sometimes saturates at high visual extinction, a correlation is clearly present for a large fraction of the measured lines of sight between these

two regimes. More precisely, the C¹⁸O, and HNC (1–0) lines are the best tracers of the visual extinctions when the integrated line intensity is above 1 K km s $^{-1}$. Indeed, there is an excellent agreement between the black line and the white line when W is above the intensity median value, and the scatter is low around these curves for both transitions. The C¹⁸O, and HNC (1–0) lines are followed by ³²SO and ¹²CS (2–1) lines. But these start to show a second twofold behavior at high visual extinction, a fraction of the pixels showing a saturation of the line integrated intensity at high visual extinction. This saturation branch is amplified for the HCN, ¹²CN, and C₂H (1–0) lines. The ¹³CO (1–0) line is also a good tracer of the visual extinction as it has a clearly monotonic (though non-linear) relationship with low scatter from $A_V \sim 2$ to $A_V \sim 20$.

The second trend concerns the visual extinction thresholds at which the lines become clearly detected. Lines that are detected over a smaller fraction of the mapped FoV show up at a higher A_V than lines with a more extended spatial distribution. Moreover, this threshold behavior is amplified when the position-position-velocity cubes are not smoothed at a common angular resolution in the first place. We emphasize two particular examples. First, the N₂H⁺ (1–0) line has a surface filling factor of 2.4% and is detected at a median visual extinction of 26, while the filling factor of the HCO⁺ (1–0) is 68% and this line is detected at a median visual extinction of 4.4, close to the median visual extinction at which ¹²CO (1–0) is emitted. Second, this A_V -threshold behavior is also clear for the suite of CO isotopologues, where ¹²CO and ¹³CO (1–0) are detected at visual extinctions even lower than one, while C¹⁸O and C¹⁷O (1–0) are mostly detected for visual extinctions above three and six, respectively. The obvious explanation is related to detection limits. Rarer isotopologues produce weaker lines per unit column density, hence require a larger total gas column density to produce a signal above the detection threshold.

However, the A_V -flat asymptotes at low values of the integrated intensities are also evidence that it is not just a detection problem. Indeed, a linear relation is expected between the visual extinction and the integrated intensity at low values, that is, in the optically thin regime. The linear trend should thus only

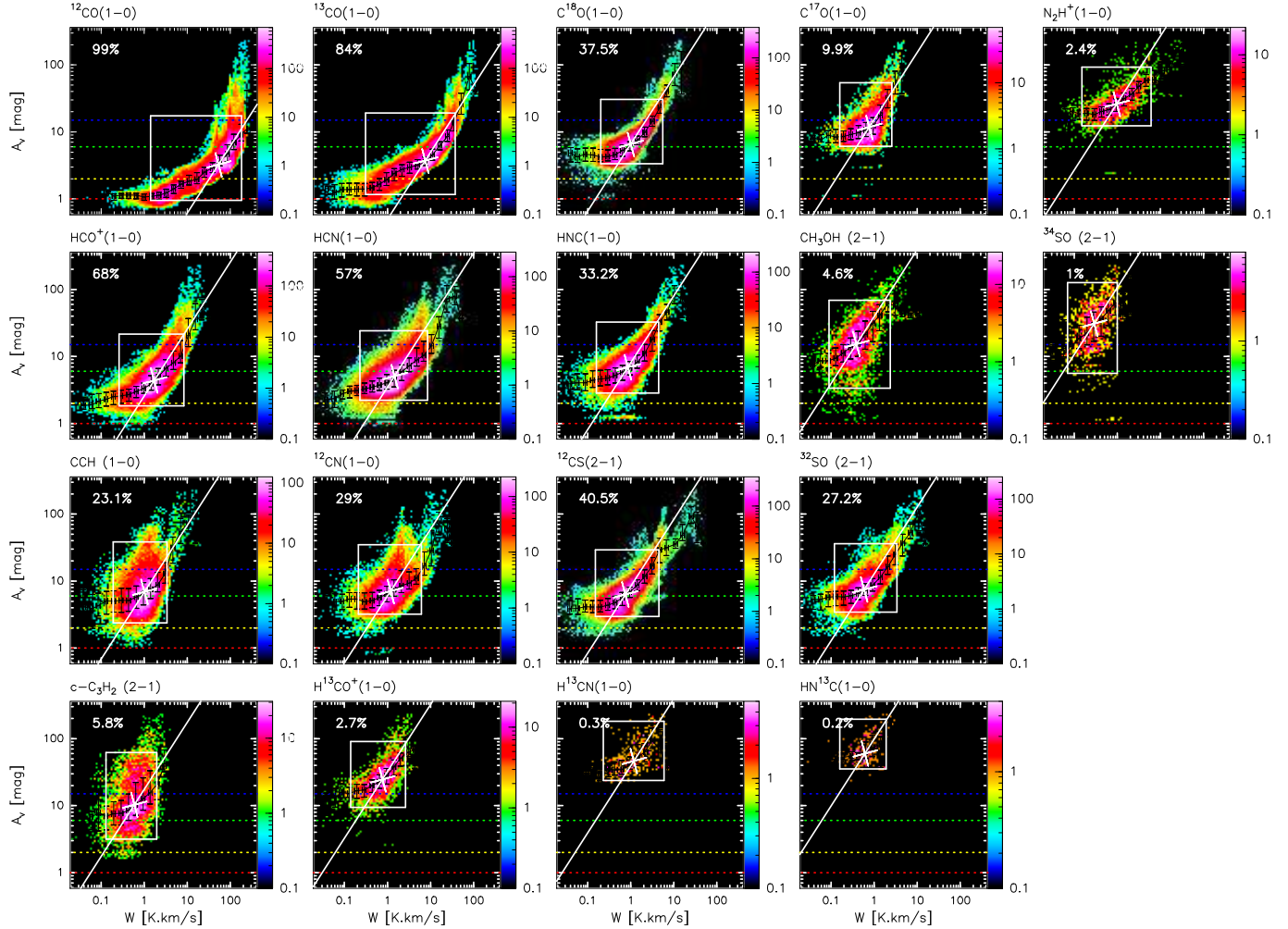


Fig. 10. Joint distributions of the visual extinction as a function of the line integrated intensity for a selection of the detected lines. The percentage in the top left corner indicates the surface over which the joint distributions can be reliably computed. These distributions contain both the global trend for the bulk of the gas and extreme behavior at low and high visual extinctions. The number of sightlines falling in a given 2D bin of the distribution is color-coded using a logarithmic scale to emphasize the extreme behavior (in particular the dense cores) that occupies a small fraction of the observed field of view. In contrast, the white rectangle displays the region of the distribution where 90% of the points are located: 2.5% of the points are outside this rectangle on each side. This allows us to define more robust global trends for the bulk of the gas. The white point shows the median of the two marginalized distributions. A line of unit slope, that is, a linear relationship between visual extinction and the line integrated intensities, is overlaid as the white plain line going through the white cross. The black points show the median values of all data points falling in a regularly sampled interval of the logarithm of the line integrated intensity. The black error bars show the range of values where 50% of the points in the current bin are located. This allows us to ask whether molecular lines are good tracers of the visual extinction. All these parameters are listed in Table 8. The red, orange, green, and blue horizontal dashed lines show the visual extinction limits (1, 2, 6, and 15 mag, respectively) used in the masks of Fig. 6. This enables us to visualize the amount of well detected pixels that falls in each of the masks for each line.

be interrupted at the detection threshold. In contrast, there is a A_V -threshold above which the species starts to emit. This is corroborated by intensity ratios that do not match the values expected from the known carbon isotope ratios, even at low visual extinction where optical depth effects are negligible. The A_V -thresholds could either be explained in terms of chemical or dynamical reasoning. Turbulent mixing between the phases of the ISM or the existence of dense but diffuse globulettes at the edge of H II regions belong to the latter category. In the former category, we have selective chemistry.

In summary, the (1–0) or (2–1) lines of molecular tracers are, to first order, sensitive to different ranges of visual extinction when detected at a similar noise level. In addition, they are, overall, well correlated with the amount of matter along the line of sight. This behavior will be quantified in a following paper concerning the PCA of the dataset (Gratier et al. 2017).

5.2. Tracer luminosities per proton

Figure 11 shows the spatial distribution of the ratio of the line integrated intensity to the visual extinction. The panels show these ratios for the molecular tracers ordered in the same way as the figure displaying the line integrated intensities (Fig. 2). We also added the spatial distribution of the visual extinction and dust temperature as the top right and bottom left panels, respectively, for reference. The intensity ratios are normalized by their median values and the intensities are displayed using a logarithmic scale symmetrically stretched around 1. This eases the visualization of departure of the ratio by a multiplicative factor, such as 1/2 and 2, for example. The luminosity per proton is easily computed by dividing the W/A_V ratios by the standard value of $N_H/A_V = 1.8 \times 10^{21} \text{ H cm}^{-2}/\text{mag}$.

Table 8. Properties of the joint distributions of visual extinction and line integrated intensities.

Species	Transition	Filling factor %	$W^{2.5\%} - W^{\text{med}} - W^{97.5\%}$ K km s ⁻¹	$A_V^{2.5\%} - A_V^{\text{med}} - A_V^{97.5\%}$ mag
¹² CO	1–0	99	1.4–53–180	0.95–3.3–17
¹³ CO	1–0	84	0.31–7.5–38	1.2–3.7–19
HCO ⁺	1–0	68	0.26–1.7–8.3	1.8–4.4–22
HCN	1–0	57	0.23–1.5–8.5	2.2–5.1–24
¹² CS	2–1	41	0.15–0.75–4.5	2.9–6.3–29
C ¹⁸ O	1–0	38	0.2–1–5.5	3.4–6.6–31
¹² CN	1–0	29	0.21–1.2–6.1	3.2–7.1–35
C ₂ H	1–0	23	0.19–1–3.4	2.4–6.9–38
³² SO	2–1	27	0.12–0.59–3.4	3.4–7.5–36
HNC	1–0	33	0.16–0.86–4.4	2.9–6.9–33
C ¹⁷ O	1–0	9.9	0.16–0.77–2.6	6.1–12–54
c-C ₃ H ₂	2–1	5.8	0.13–0.59–2	3.2–10–62
CH ₃ OH	2–1	4.6	0.089–0.39–2.4	3.4–15–69
H ¹³ CO ⁺	1–0	2.7	0.14–0.76–2.6	9.4–25–91
N ₂ H ⁺	1–0	2.4	0.15–0.97–6.1	12–26–93
³⁴ SO	2–1	1	0.07–0.29–1	5.6–31–130
H ¹³ CN	1–0	0.32	0.23–1.2–5.9	24–46–180
HN ¹³ C	1–0	0.18	0.16–0.61–1.9	35–60–190

Notes. The lines are sorted by decreasing value of their surface filling factor.

The $W(^{12}\text{CO})/A_V$ and $W(^{13}\text{CO})/A_V$ present a similar pattern, that is, a luminosity per proton higher than the median value in translucent gas and lower in dense gas. The luminosity per proton decreases again at the very edge of the molecular cloud. The $W(\text{C}^{18}\text{O})/A_V$ ratio shows less variation by a factor of two to three. The $W(\text{HCO}^+)/A_V$, $W(\text{HCN})/A_V$, $W(\text{HNC})/A_V$, and $W(^{12}\text{CN})/A_V$ ratios show maxima associated with the Orion B Eastern edge and with the NGC 2024 H II bubble. The dark filament in front of NGC 2024 delineates the frontier between ratios higher/lower than the median. This can be interpreted as an excitation effect due to higher electron density or an abundance effect. The west/east asymmetry of the ratio is more marked for the $W(\text{C}_2\text{H})/A_V$ ratio, in particular around the NGC 2023 region. The $W(^{12}\text{CS})/A_V$ shows a specific pattern with a maximum at the center of NGC 2024 and a minimum between NGC 2024 and NGC 2023.

5.3. Typical abundances

As the low- J molecular lines are, overall, well correlated to the column density of molecular gas, the luminosities per proton could, in principle, be used to estimate the abundance of the different species. To do this, we computed the column density of each species, N_{species} , that is required to produce an integrated intensity of 1 K km s⁻¹ assuming that the gas is at local thermal equilibrium. The values of N_{species} vary by less than 20% when the temperature increases from 20 to 30 K. Typical abundances with respect to the proton number can then be computed with

$$[\text{species}] = \frac{W}{A_V} \frac{A_V}{N_H} \frac{N_{\text{species}}}{1 \text{ K km s}^{-1}}. \quad (8)$$

Table 9 lists the minimum, maximum, and median values of the so-called abundances for each line. The deduced abundances are reasonable for all the studied lines except ¹²CO (1–0), which delivers abundances that are too low by one order of magnitude because this line is highly optically thick.

Table 9. Minimum, median, and maximum values of the abundances derived for each species.

Species	Transition	$(W/N_H) \times (N_{\text{species}}/1 \text{ K km s}^{-1})$
		[Pseudo-Abundance] min–med–max
¹² CO	1–0	$1 \times 10^{-7} - 1 \times 10^{-5} - 3 \times 10^{-5}$
¹³ CO	1–0	$1 \times 10^{-7} - 1 \times 10^{-6} - 4 \times 10^{-6}$
C ¹⁸ O	1–0	$2 \times 10^{-8} - 1 \times 10^{-7} - 1 \times 10^{-6}$
C ₂ H	1–0	$1 \times 10^{-9} - 1 \times 10^{-8} - 1 \times 10^{-7}$
C ¹⁷ O	1–0	$1 \times 10^{-8} - 5 \times 10^{-8} - 4 \times 10^{-7}$
CH ₃ OH	2–1	$1 \times 10^{-10} - 1 \times 10^{-9} - 3 \times 10^{-8}$
³² SO	2–1	$1 \times 10^{-10} - 1 \times 10^{-9} - 5 \times 10^{-9}$
¹² CN	1–0	$2 \times 10^{-10} - 2 \times 10^{-9} - 2 \times 10^{-8}$
HCN	1–0	$1 \times 10^{-10} - 1 \times 10^{-9} - 4 \times 10^{-9}$
¹² CS	2–1	$1 \times 10^{-10} - 4 \times 10^{-10} - 5 \times 10^{-9}$
c-C ₃ H ₂	2–1	$2 \times 10^{-11} - 3 \times 10^{-10} - 3 \times 10^{-9}$
HCO ⁺	1–0	$4 \times 10^{-11} - 3 \times 10^{-10} - 2 \times 10^{-9}$
N ₂ H ⁺	1–0	$2 \times 10^{-11} - 2 \times 10^{-10} - 3 \times 10^{-9}$
HNC	1–0	$3 \times 10^{-11} - 2 \times 10^{-10} - 2 \times 10^{-9}$
H ¹³ CO ⁺	1–0	$1 \times 10^{-11} - 3 \times 10^{-11} - 4 \times 10^{-10}$

Notes. The lines are sorted by decreasing value of the median pseudo-abundance.

6. Line ratios as tracers of different physico-chemical regimes

Line intensity ratios are commonly used to study the physical and chemical properties of the gas in different environments. The advantage of using line ratios instead of absolute line intensities is that this method allows removal of calibration uncertainties (when lines are observed simultaneously). It is then easier to compare one source to another. Line ratios may also remove

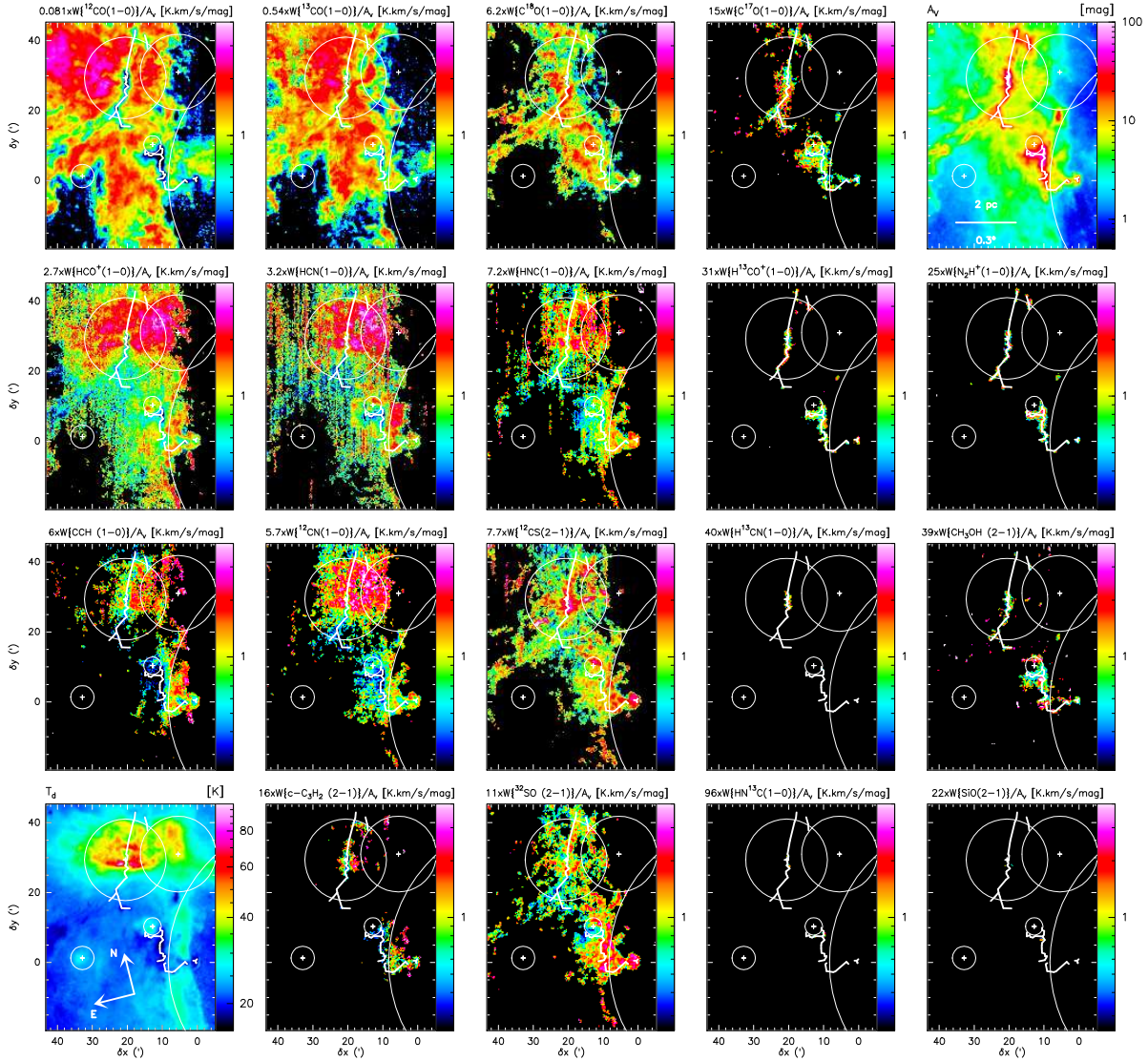


Fig. 11. Spatial distribution of the ratio of the line integrated intensity to the visual extinction for some of the detected lines in the 3mm band, plus the dust temperature (bottom left panel) and the visual extinction (top right corner). The ratios are normalized by their median value that hence appears as 1 on the color look-up table. The color scale shows ratio values between 0.25 and 4 times the median value for all the ratio panels.

excitation effects and bring forward actual chemical variations. Our knowledge of the chemistry of the gas then allows us to use line ratios to constrain the physical properties of the gas.

An important basic property we wish to determine easily from observations is the density of the gas. Forming dense gas is a required step of star formation, and the availability to form dense gas may regulate star formation efficiency (Lada et al. 2013). Line ratios of HCN and HCO⁺ with respect to ¹²CO and ¹³CO are commonly used to trace the fraction of dense gas in galactic and extragalactic GMCs (e.g., Lada et al. 2012). This is because ¹²CO and ¹³CO can be excited at low densities ($\sim 10^2 \text{ cm}^{-3}$) compared to HCN and HCO⁺, which are expected to be excited only at high densities ($\sim 10^5 \text{ cm}^{-3}$). Indeed, the HCN/¹²CO ratio is observed to be well correlated with the star-formation efficiency, traced by IR/HCN in M 51 (e.g., Bigiel et al. 2016).

In this section we first show line ratios involving the brightest detected lines, that is, ¹²CO and ¹³CO (1–0), and we conclude with a few other interesting ratios. For this, we discuss 2D-histograms of the ratio denominator vs. the ratio numerator, the spatial distribution of the ratios, and the 2D-histogram of the

ratio vs. the visual extinction. This will allow us to study the correlations present before computing the ratio, in order to visually assess the correlations of the line ratios with different kinds of regions, and to quantitatively study potentially remaining correlations with the visual extinction.

6.1. Ratios with respect to ¹²CO and ¹³CO (1–0)

The 2D-histograms shown in Fig. 12 display the relation of the integrated intensity of different lines as a function of the integrated intensity of the ¹²CO (1–0) line. While the eye is mainly caught by the saturation of the ¹²CO line, that is, other tracer intensities increase by a large factor when $W(^{12}\text{CO}) \sim 100\text{--}200 \text{ K km s}^{-1}$, most of the data follows a different trend. The running median and running interval containing 50% of the data, materialized as black points and error bars, indicate that most of the tracers have first a relatively constant integrated intensity as $W(^{12}\text{CO})$ increases, and then their integrated intensity is well correlated to $W(^{12}\text{CO})$. As shown by the white rectangles that display the part of the 2D-histogram populated by 90% of the points, most of the tracers only emit when the ¹²CO (1–0)

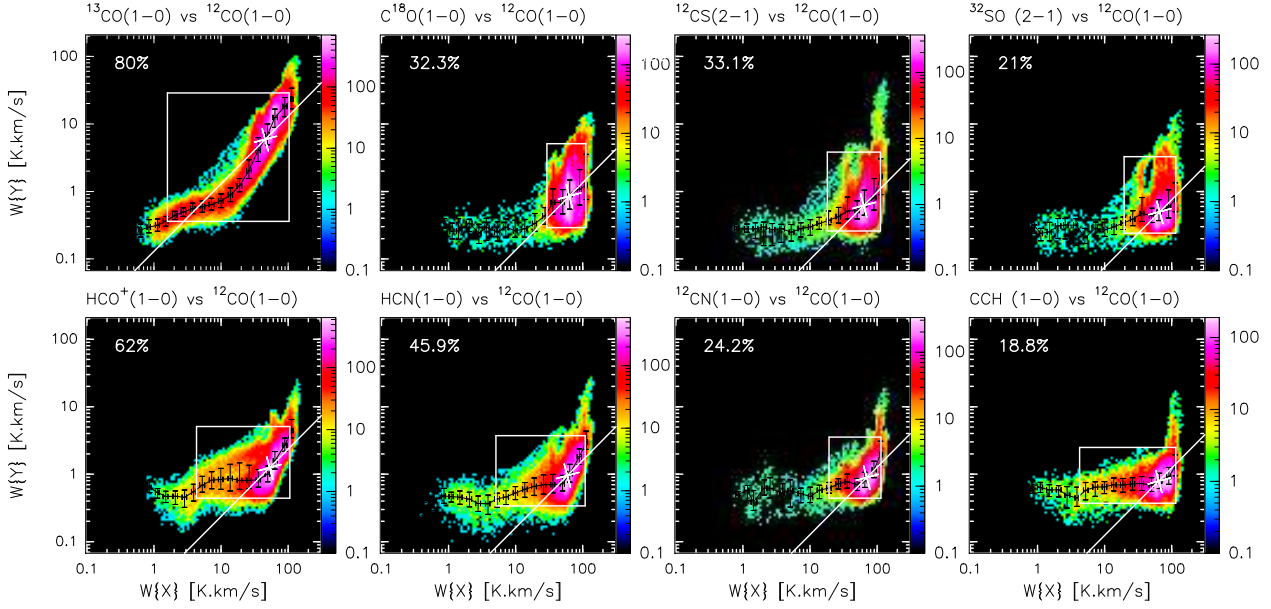


Fig. 12. Joint distributions of various line intensities integrated over $[9, 12 \text{ km s}^{-1}]$. Markers have the same signification as in Fig. 10. The x -axis is always $W\{^{12}\text{CO}(1-0)\}$.

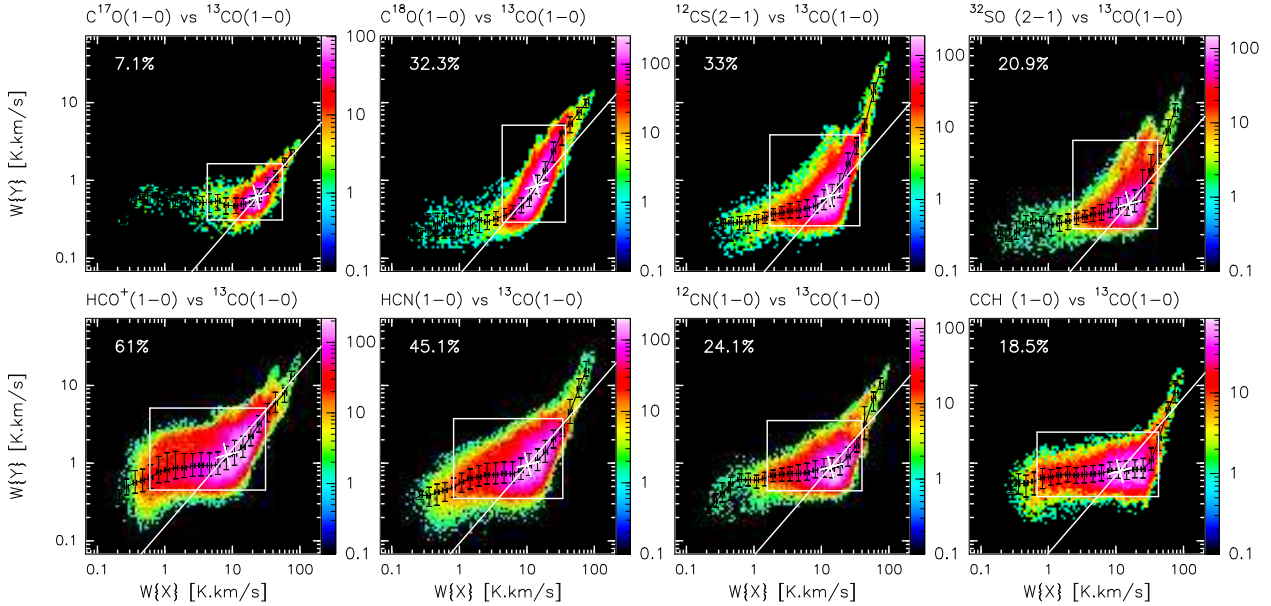


Fig. 13. Same as Fig. 12, except that the x -axis is now $W\{^{13}\text{CO}(1-0)\}$.

line is already relatively bright at $\sim 10-20 \text{ K km s}^{-1}$. On the other hand, the CCH, HCN, HCO⁺, and ¹³CO (1-0) lines show a significant fraction of the data at ¹²CO (1-0) integrated intensity between 1 and 10 K km s^{-1} . The ¹³CO (1-0) line has a specific behavior as it is under-luminous with respect to a linear correlation going through the median behavior at intermediate ¹²CO (1-0) intensities ($5 \lesssim W(^{12}\text{CO}) \lesssim 30 \text{ K km s}^{-1}$).

Figure 13 shows the same 2D-histograms as before but with respect to $W(^{13}\text{CO})$. In general, the same trends seen for ¹²CO are seen for ¹³CO. The species integrated intensities have a relatively constant or slightly increasing integrated intensity as $W(^{13}\text{CO})$ increases up to $\sim 10 \text{ K km s}^{-1}$. Their intensity is then well correlated to $W(^{13}\text{CO})$. The effects of the ¹³CO (1-0) saturation are visible but less pronounced than with respect to the ¹²CO (1-0) line.

Figure 14 presents the spatial distribution of the line ratios involving ¹²CO. The ratios are normalized by their median value to emphasize the symmetric departure of the ratios compared to the general trend. The ratios all show minimum values in the dense regions associated with NGC 2024, NGC 2023, and Horsehead. This probably reflects the saturation of the ¹²CO emission in regions with the highest column density. These regions are also the densest regions, which implies that the molecular tracers are easily produced and excited. As the ¹²CO line becomes saturated, the available energy gets carried away by other ¹²CO transitions or other molecular species. A west-east gradient is superimposed on the first pattern for the ratios involving HCO⁺, HCN, C₂H, ¹²CN, and HNC (not shown), for both ¹²CO and ¹³CO. The minimum values are obtained on the western edge; the maximum values in the eastern diffuse

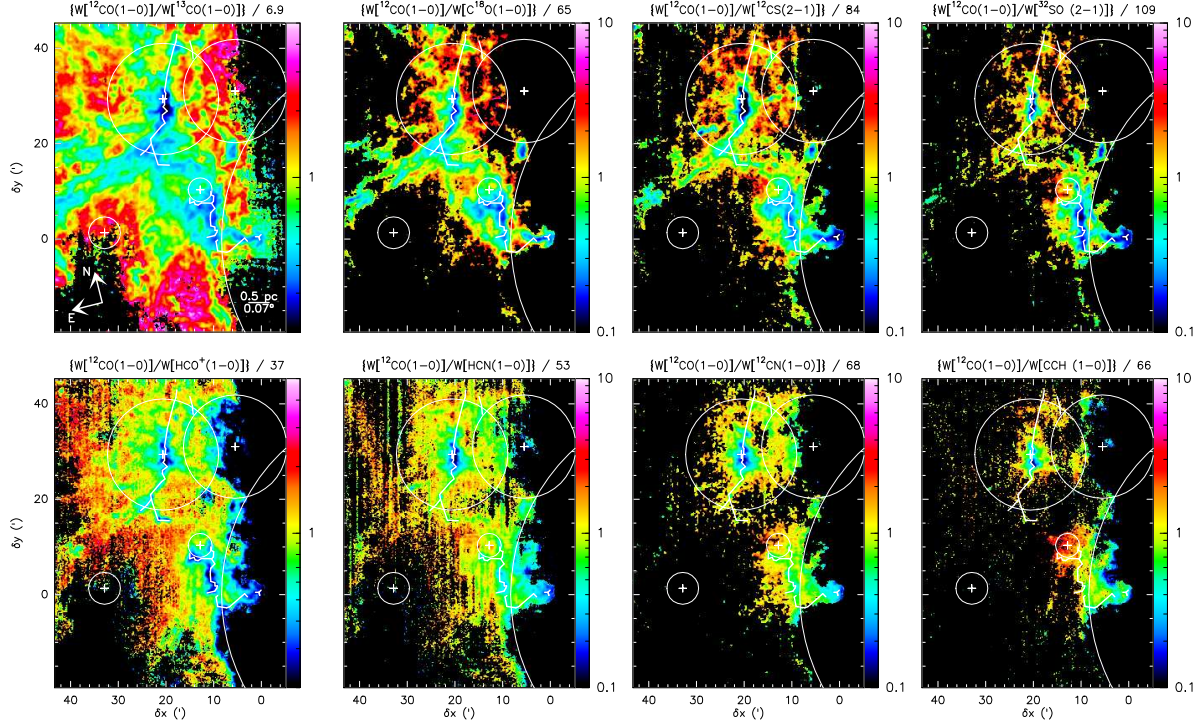


Fig. 14. Spatial distribution of the ratios of line intensity integrated over $[9, 12 \text{ km s}^{-1}]$. The ratios are normalized by the median value of the ratio. The numerator is always $W\{^{12}\text{CO}(1-0)\}$. The color scale shows ratio values between 0.1 and 10 for all the ratio panels, except the $^{12}\text{CO}/^{13}\text{CO}$ and $^{12}\text{CO}/\text{HCO}^+$ panels where the color scale goes from 0.2 to 5.

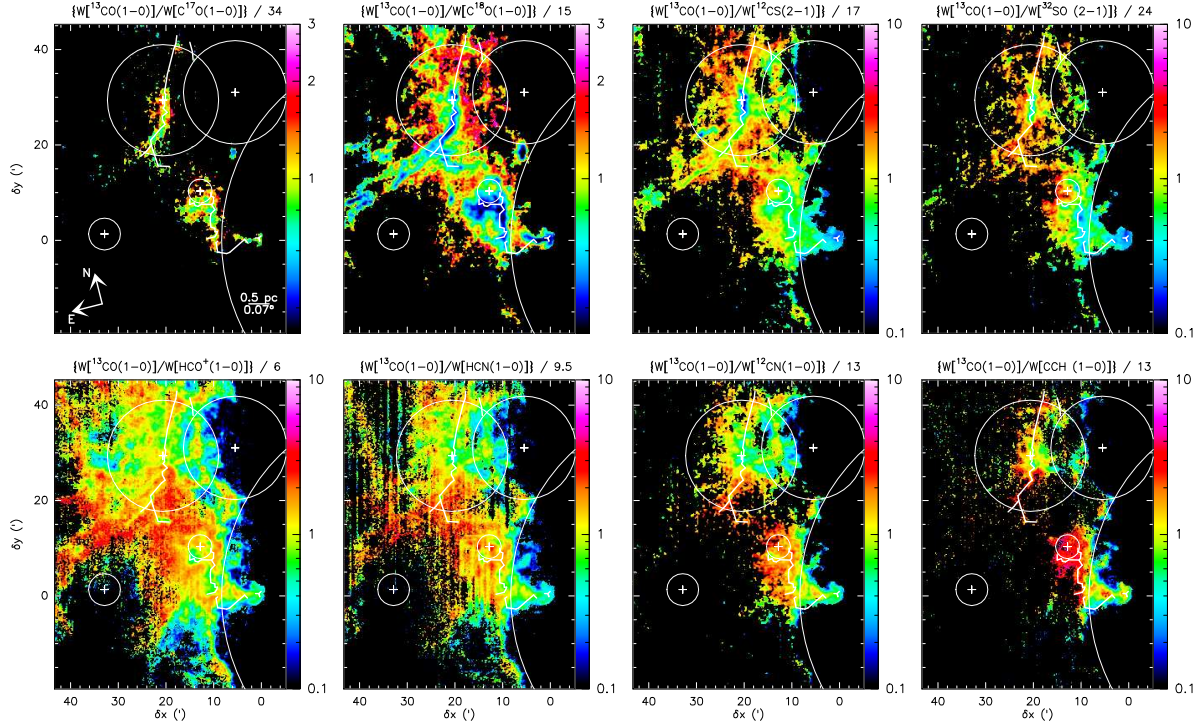


Fig. 15. Same as Fig. 14, except that the numerator is now $W\{^{13}\text{CO}(1-0)\}$. The color scale shows ratio values between 0.1 and 10 for all the ratio panels, except the $^{13}\text{CO}/\text{C}^{17}\text{O}$ and $^{13}\text{CO}/\text{C}^{18}\text{O}$ panels where the color scale goes from 0.33 to 3.

region. This pattern probably indicates a gradient in excitation and abundance in UV-illuminated regions for molecules sensitive to the far-UV radiation. Finally an approximately circular structure around NGC 2024 with a luminosity deficit in C^{18}O , ^{12}CS , and marginally ^{32}SO probably traces UV-illuminated material near NGC 2024.

Similar spatial behavior is also seen for the ratios with respect to ^{13}CO (1-0) (see Fig. 15), but slightly attenuated because the saturation of the ^{13}CO (1-0) line is less pronounced. The first pattern (minimum ratio values in regions of highest density) for the ratios including C^{18}O , ^{12}CS , and ^{32}SO supports the interpretation in terms of opacity for the densest/brightest regions.

Table 10. Minimum, median, and maximum values of the ratios of diverse line integrated intensities.

Species #1	Trans.	Species #2	Trans.	$W(\#1)/W(\#2)$ min-med-max
^{12}CO	1–0	^{13}CO	1–0	1.2–6.9–46
^{12}CO	1–0	HCO^+	1–0	1.6–37–140
^{12}CO	1–0	C^{18}O	1–0	2.9–65–410
^{12}CO	1–0	^{12}CN	1–0	1.9–68–210
^{12}CO	1–0	C_2H	1–0	1.8–66–320
^{12}CO	1–0	HNC	1–0	1.8–66–320
^{12}CO	1–0	^{12}CS	2–1	2.4–84–350
^{12}CO	1–0	^{32}SO	2–1	2.7–110–400
^{13}CO	1–0	HCO^+	1–0	0.16–6–30
^{13}CO	1–0	C_2H	1–0	0.4–13–91
^{13}CO	1–0	^{12}CN	1–0	0.47–13–57
^{13}CO	1–0	C^{18}O	1–0	0.57–15–50
^{13}CO	1–0	HNC	1–0	0.4–13–91
^{13}CO	1–0	^{12}CS	2–1	0.71–17–70
^{13}CO	1–0	^{32}SO	2–1	0.67–24–98
^{13}CO	1–0	C^{17}O	1–0	0.65–34–85
HNC	1–0	^{12}CN	1–0	0.33–1.7–6.4
^{12}CS	2–1	HNC	1–0	0.22–1.1–7.3
^{12}CN	1–0	HNC	1–0	0.22–1.1–3.9
C^{18}O	1–0	^{12}CS	2–1	0.14–1.2–6.2
C^{18}O	1–0	HNC	1–0	0.16–1.3–8.5
HCN	1–0	^{12}CN	1–0	0.33–1.7–6.4
HCO^+	1–0	HCN	1–0	0.33–1.7–6.4
HCN	1–0	HNC	1–0	0.33–1.7–6.4
HCO^+	1–0	HNC	1–0	0.33–1.7–6.4
C^{18}O	1–0	C^{17}O	1–0	0.43–4.3–8.6
HCO^+	1–0	N_2H^+	1–0	0.33–1.7–6.4

Notes. In each group, the lines are sorted by increasing value of the $W(\#1)/W(\#2)$ median.

The east-west pattern is even more pronounced for the HCO^+ species with an excess emission of the molecular tracers in the UV-illuminated regions and a deficit in the diffuse/translucent gas. This may be a combined effect of lower heating, moderate density, and an increase of ^{13}CO due to isotopic fractionation ($^{12}\text{CO} + ^{13}\text{C}^+ \rightarrow ^{13}\text{CO} + ^{12}\text{C}^+$). Finally, the east-west pattern does not reach the translucent regions on the eastern side for C_2H , and CN . In these cases, we mostly see the increase of the line ratio in the high extinction gas, including the compressed western edge (Schneider et al. 2013).

Finally, Fig. 16 shows the 2D-histograms of A_V as a function of the line ratios involving ^{12}CO . The line ratios have a bimodal behavior relative to A_V , with values lower than the median (marked by the white cross) found both for high- and low- A_V regions. Values of the ratios higher than the median are associated with a small range of visual extinctions, either the translucent ($2 < A_V < 6$) or filamentary ($6 < A_V < 15$) gas. The bimodal trend is present in all ratios, but more pronounced for those involving lines presenting an extended emission ($^{13}\text{CO}/^{12}\text{CO}$ and $\text{HCO}^+/^{12}\text{CO}$).

The increasing branch ($\text{in } A_V$) is the dominating one for the ratios involving ^{13}CO , C^{18}O , ^{12}CS , ^{32}SO , and ^{12}CN . This means that the other decreasing branch, while existing, represents a small number of points in our FoV. Low values of these ratios thus mostly point to high-density regions. The increasing branch is most likely a consequence of the saturation of the ^{12}CO (1–0)

line compared to the other lines at large gas column densities. In addition, many molecular species will become more abundant at large column densities, as they become shielded from UV-radiation. Both effects will produce lower ratios at large A_V . Because all tracers are correlated to first order to the column density, one would expect to remove a correlation with A_V by taking the ratio of two lines. However, a (anti-)correlation may remain. This is due to the fact that the correlation between the integrated intensity of weaker lines and $W(^{12}\text{CO})$ have a non-linear behavior, probably because these lines have a lower opacity than the ^{12}CO (1–0) line for large gas column densities.

In contrast, the decreasing branch dominates for the ratios involving the HCO^+ , HCN , and C_2H (1–0) lines. Low values of these ratios point to the lower visual extinction range. This is clear for $^{12}\text{CO}/\text{C}_2\text{H}$, whose running median almost monotonically increases from an A_V of ~ 2 to 10 mag. When the $^{12}\text{CO}(1-0)/\text{HCO}^+(1-0)$ and $^{12}\text{CO}(1-0)/\text{HCN}(1-0)$ ratios increase, the running median of the visual extinction first increases from values lower than 2 mag up to ~ 8 mag, and it then starts to decrease again. One interesting result is that all decreasing branches sample values of the visual extinction as low as 1–2 mag. This is consistent with the fact that all the associated species are detected in diffuse clouds through absorption against extra-galactic continuum sources (Lucas & Liszt 1996, 2000; Liszt & Lucas 2001). This probably means that the strongly polar species, C_2H , and HCO^+ , reach a radiative regime where they emit more efficiently than ^{12}CO , the weak excitation regime described by Liszt & Pety (2016).

Figure 17 shows the 2D-histograms of the visual extinction as a function of the ratio involving ^{13}CO . We see similar global results as for ^{12}CO , that is, a globally constant visual extinction at values of the ratio higher than the median, and an increasing and a decreasing A_V branch when the ratio decreases below the median value. In contrast with the ratios involving ^{12}CO (1–0), the decreasing A_V branch dominates for most of the ratios. Indeed, the running median for all ratios except $\text{C}^{18}\text{O}/^{13}\text{CO}$ decrease for low visual extinctions. The decrease is even almost monotonic for ratios involving the HCO^+ , C_2H , ^{12}CN , and HCN (1–0) lines. This behavior is consistent with the fact that the correlation between the integrated intensity of the different species and $W(^{13}\text{CO})$ is more linear. Taking the ratios thus better removes the correlations with the gas column density.

6.2. Various other line ratios

Figures 18 to 20 show the same plots as the previous section but for other line ratios including tracers of the column density (C^{18}O , ^{12}CS , and HNC), and other highly studied ratios in extra-galactic observations (HCO^+ , HCN , HNC , and CN).

The 2D-histograms that display the integrated intensity of C^{17}O , HNC , and ^{12}CS with respect to $W(\text{C}^{18}\text{O})$ show two main behaviors (see Fig. 19). The C^{17}O , HNC , and ^{12}CS (2–1) lines are over-luminous compared to the C^{18}O (1–0) line at low intensities. Their intensities then become linearly correlated. In addition, the ^{12}CS (2–1) line becomes much brighter than both the C^{18}O and HNC (1–0) lines at high-intensity values. The integrated brightnesses of the $\text{HCN}-\text{HCO}^+$, $\text{HNC}-\text{HCO}^+$, $\text{HNC}-\text{CN}$, and $\text{HNC}-\text{HCN}$ (1–0) line pairs are all linearly correlated. The best correlation is found for the $\text{HCN}-\text{CN}$ pair of lines.

Describing the spatial patterns of the ratios shown in Fig. 19 is less straightforward because the fraction over the FoV where the two lines are detected at enough signal-to-noise ratio is

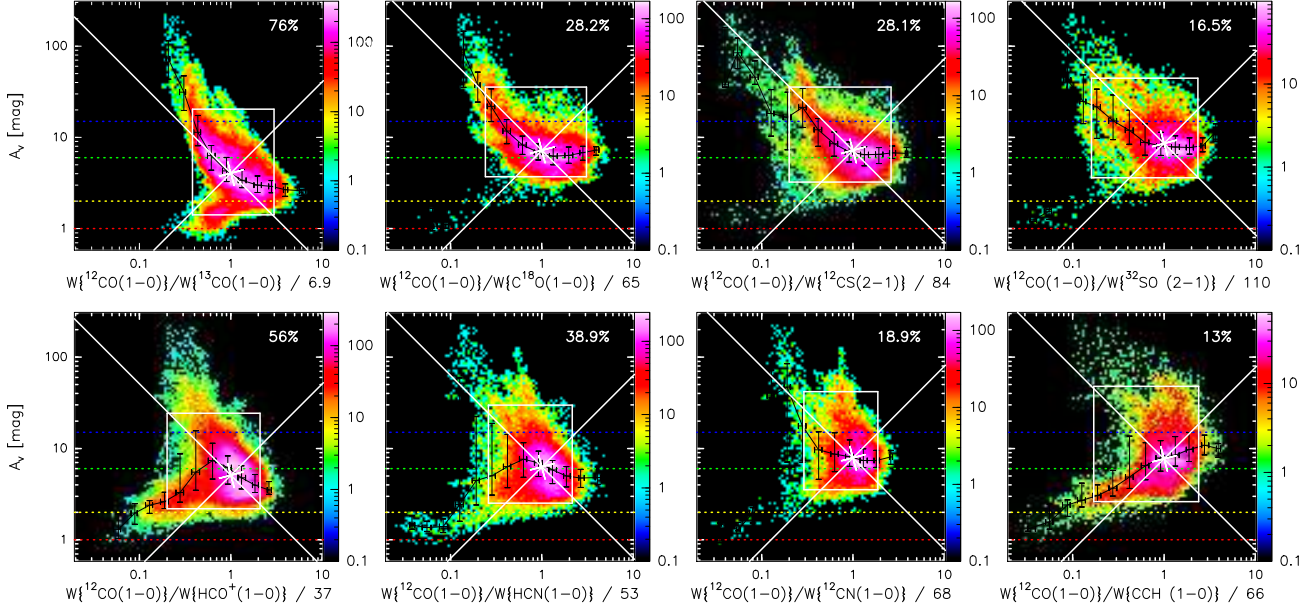


Fig. 16. Joint distributions of the visual extinction as a function of the ratios of line integrated intensities. The ratios are normalized by their median value. The ratio numerator is always here $W\{^{12}\text{CO}(1-0)\}$. Markers have the same signification as in Fig. 10.

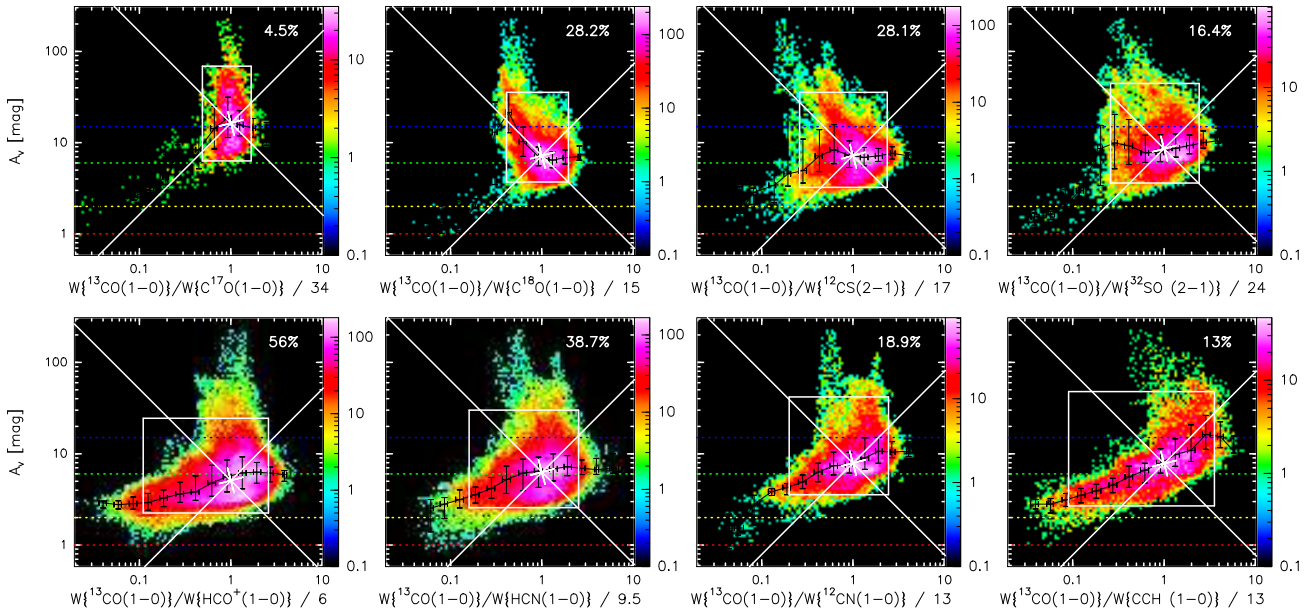


Fig. 17. Same as Fig. 16, except that the ratio numerator is now $W\{^{13}\text{CO}(1-0)\}$.

lower. The $\text{C}^{18}\text{O}/\text{C}^{17}\text{O}$ ratio, shown in the upper left panel, is fairly flat with no clear spatial pattern. The east-west pattern is particularly marked on the $\text{C}^{18}\text{O}/^{12}\text{CS}$ and $\text{HNC}/\text{C}^{18}\text{O}$ ratios. The $^{12}\text{CS}/\text{HNC}$, $^{12}\text{CN}/\text{HNC}$, and HCN/HNC ratios all show an approximately circular structure around NGC 2024 with a deficit of HNC integrated intensity. We relate the latter behavior to an isomerisation of HNC into HCN when the gas temperature increases.

Computing the ratio for these lines removed almost any linear (anti-)correlation with the visual extinction, except for the HCN/HNC and CN/HNC ratios (see Fig. 20). For the filamentary gas (A_v between 6 and 15 mag) the ratio spans a large range of values, up to one order of magnitude for $\text{C}^{18}\text{O}/^{12}\text{CS}$ and $\text{C}^{18}\text{O}/\text{HNC}$.

7. Discussion

7.1. Typical line intensities in a strongly UV-illuminated part of a GMC

The FoV sampled here is not a random one square degree part of any GMC. The left panels of Fig. 21 show the spatial distribution of the visual extinction and dust temperature over a much larger fraction of the Orion B molecular cloud than the one presented in this paper, which is shown as the black rectangle. The right panels compare the PDFs of dust properties over our FoV with the PDFs of two other regions with the same surface area. Table 11 lists the minimum, median, and maximum values of the associated distributions, as well as their 5 and 95% quantiles. This clearly shows that three different kinds of environment

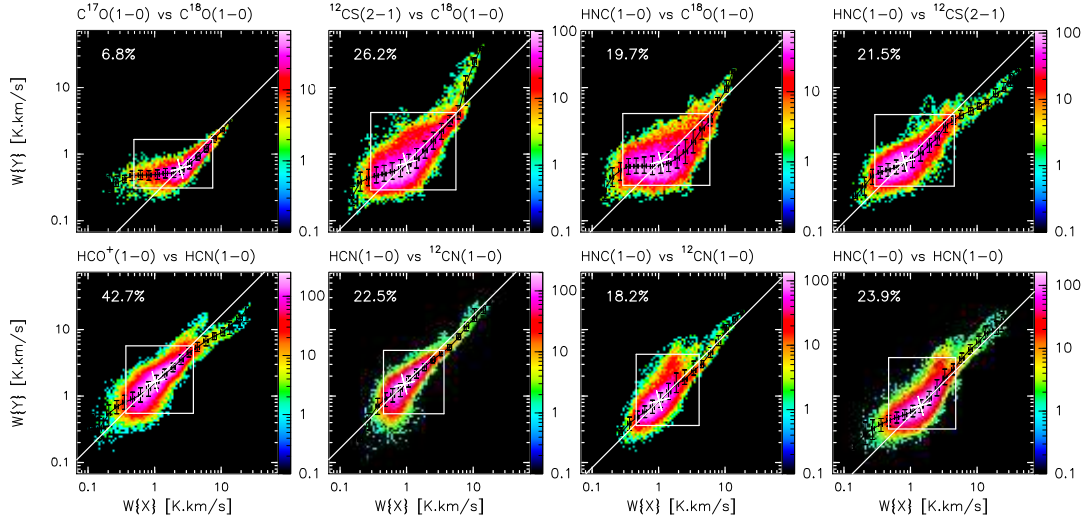


Fig. 18. Same as Fig. 12, except that there is no common x -axis in this figure.

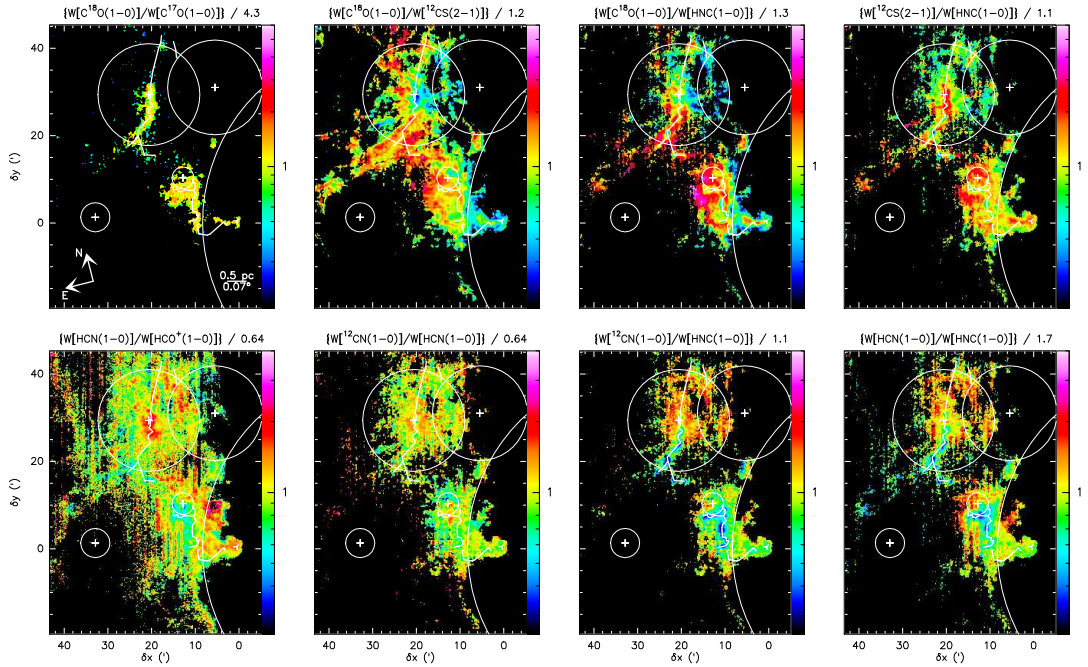


Fig. 19. Same as Fig. 14, except that there is no common numerator in this figure.

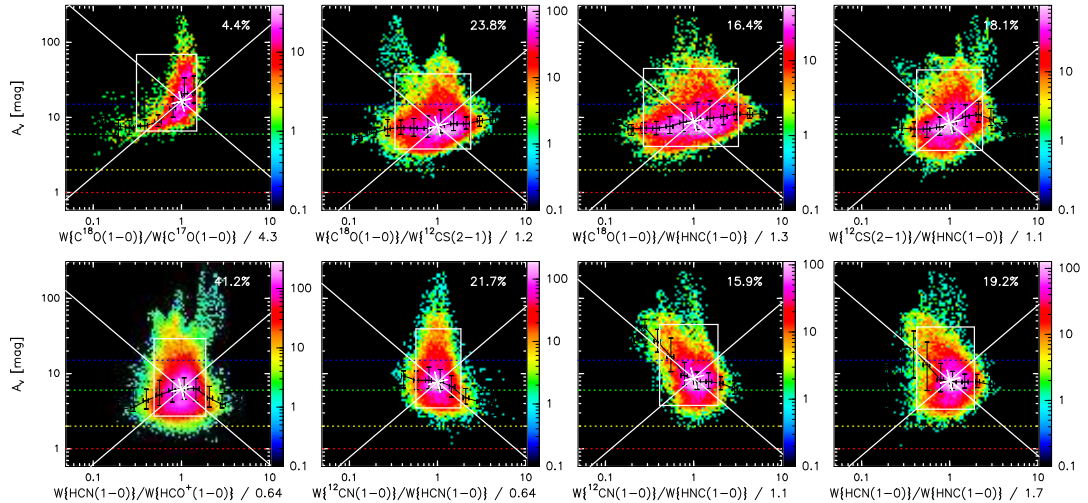


Fig. 20. Same as Fig. 14, except that there is no common ratio numerator in this figure.

Table 11. Visual extinction, dust temperature, and far UV illumination for three different regions of 1 square-degree area in Orion B.

Environment	$A_V^{\min} - A_V^{5\%} - A_V^{\text{med}} - A_V^{95\%} - A_V^{\max}$ mag	$T_d^{\min} - T_d^{5\%} - T_d^{\text{med}} - T_d^{95\%} - T_d^{\max}$ K	$G_0^{\min} - G_0^{5\%} - G_0^{\text{med}} - G_0^{95\%} - G_0^{\max}$ ISRF (Habing 1968)
UV illuminated	0.76–1–3.3–12–230	16.4–20.1–24.1–40.5–101	4.4–12–30–400–38 000
Translucent	1.1–1.5–2.4–3.5–7.7	16–17.2–17.9–18.6–20.3	3.9–5.6–6.9–8.1–13
UV shied	1.5–2.2–3.4–7.9–34	12.9–15.2–17.1–18.5–20.3	1.3–3–5.3–8–13

exist in the Orion B molecular cloud. First, the lowest dust temperatures are associated with relatively high visual extinctions (red rectangle). Second, the blue rectangle identifies a translucent region (all pixels have $A_V \lesssim 8$), associated with a typical dust temperature of approximately 18 K. In both cases, the distribution of visual extinction and dust temperature are single peaked with a narrow full width at half maximum. In contrast, our FoV displays wide A_V and T_d distributions, and is associated with the highest dust temperatures with a median value of ~ 24 K ($G_0 \sim 30$). The presence of high gas temperatures is confirmed by the large ^{12}CO (1–0) peak temperatures that are lower limits of the kinetic temperature (Orkisz et al. 2017). These properties are associated with the presence of at least four H II regions (see Sect. 2.1) that imply a large UV-illumination (see the fourth column of Table 11). In particular, the minimum dust temperature in our field (16.4 K) is rather high in Orion B compared to the Taurus molecular cloud (Marsh et al. 2014).

Table 3 indicates that, under these sampling conditions and at the typical sensitivity achieved in studies of nearby galaxies ($3\sigma = 1 \text{ K km s}^{-1}$), only the (1–0) line of ^{12}CO , ^{13}CO , HCO^+ , HCN would easily be detected by a single-dish radio-telescope of 30 m-diameter with a single-beam receiver. A ten times better sensitivity (100 longer integration) is required to detect the (1–0) or (2–1) lines of HCN , CN , C^{18}O , ^{12}CS , C_2H , HNC , ^{32}SO , C^{17}O , and $\text{c-C}_3\text{H}_2$. Finally, another order-of-magnitude increase of the sensitivity ($3\sigma = 0.01 \text{ K km s}^{-1}$) would be needed to detect N_2H^+ , CH_3OH , H^{13}CO^+ , and H^{13}CN . This means that detecting rare isotopologues of HCO^+ , HCN , or HNC in nearby galaxies is difficult to achieve with a single-dish radio-telescope because of the dilution of the signal in the beam.

7.2. The influence of the UV field on the determination of molecular mass

The average visual extinction and CO integrated intensity for the observed FoV are 4.7 mag and 61 K km s^{-1} . This turns into a $W_{\text{CO}}/A_V = 13.0 \text{ K km s}^{-1}/\text{mag}$, while the standard X_{CO} factor, that is, $2 \times 10^{20} \text{ H}_2 \text{ cm}^{-2}/(\text{K km s}^{-1})$, corresponds to $4.7 \text{ K km s}^{-1}/\text{mag}$ when we assume a standard N_{H}/A_V factor and fully molecular gas. The HI emission indicates that diffuse gas accounts for approximately 1 mag of extinction towards Orion B (see Sect. 3.4). Assuming that contribution from atomic hydrogen to the mass is negligible towards the mapped FoV overestimates the dust-traced molecular mass by 27%, increasing the discrepancy between the CO and dust-traced mass. Therefore, we neglect this subtlety and directly compare the CO and dust-traced mass. We find that the CO-traced mass (and thus the associated surface and volume density) is approximately three times higher than the dust-traced mass.

The origin of this discrepancy lies in the intense UV illumination of the gas by massive stars. The bottom left panel of Fig. 22 compares the spatial distribution of the CO integrated intensity per visual extinction. The standard value of $4.7 \text{ K km s}^{-1}/\text{mag}$ corresponds to the transition between yellow

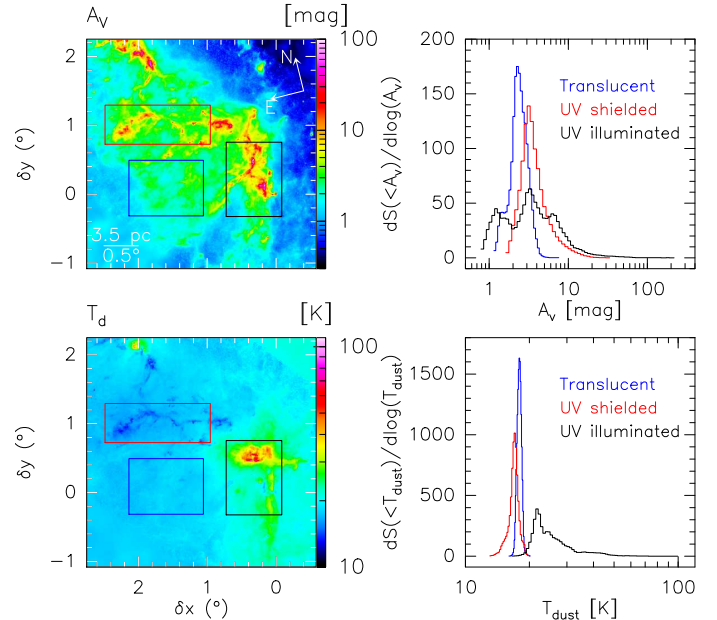


Fig. 21. Left panels: spatial distribution of the visual extinction and of the dust temperature. Right panels: probability distribution functions (PDFs) of the visual extinction and the dust temperature for the regions inside the black, blue, and red rectangles, respectively.

and green. Only diffuse gas or the UV-shielded dense gas have X_{CO} values close to or lower than standard. This is confirmed by the joint distribution of the W_{CO} and A_V where most of the points (lines of sight with $2 \lesssim A_V \lesssim 15$) lie above the white line of slope $4.7 \text{ K km s}^{-1}/\text{mag}$. When the visual extinction increases, the CO intensity saturates. At the lowest visual extinction ($A_V \lesssim 2$), CO is destroyed, giving C^+ . The spatial distribution of G_0 clearly shows that most of the gas lies in regions with $G_0 > 10$, the mean value of G_0 being 45. Under such conditions, dust and gas are heated to higher temperatures than in the standard interstellar radiation field. In the physical conditions of Orion B, the CO emission per H_2 molecule is increasing with the kinetic temperature, leading to a possible bias in the mass determination. The bottom right panel of Fig. 22 shows that the CO intensity per A_V increases with G_0 .

While it is tempting to conclude that only the CO-traced mass is widely overestimated in such conditions, the dust-traced mass is in fact also underestimated, as indicated by the range of virial mass that we estimated from the FoV size and CO linewidth (see Table 2). It is known that using a single dust temperature to fit the spectral energy distribution on a line of sight that contains dust at different temperatures hides the presence of cold dust along the line of sight, because the luminosity of dust increases extremely quickly with its temperature (Shetty et al. 2009).

All in all, the typical volume density we infer for the regions between 200 and $600 \text{ H}_2 \text{ cm}^{-3}$, is typical of galactic

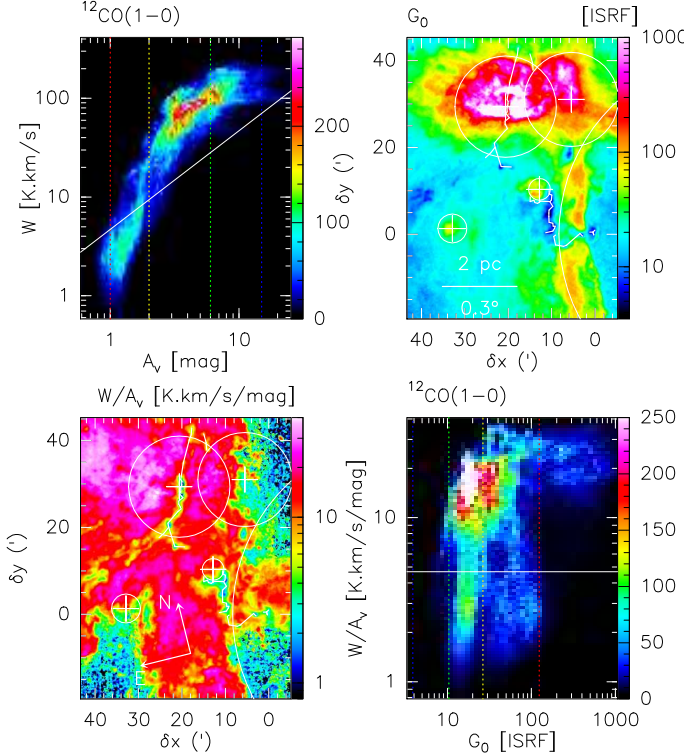


Fig. 22. *Top, left panel:* joint distribution of the ^{12}CO (1–0) line integrated intensity as a function of the visual extinction. The number of sightlines falling in a given 2D bin of the distribution is color-coded using a linear scale to emphasize the bi-modal nature of the distribution. The white line shows the location of points that follows $N(\text{H}_2) = X_{\text{CO}} W$. The red, orange, green, and blue vertical dashed lines show the visual extinction limits (1, 2, 6, and 15 mag, respectively) used in the masks of Fig. 6. *Top, right panel:* spatial distribution of the far UV illumination in units of the ISRF (Habing 1968). *Bottom, left panel:* ratio of the ^{12}CO (1–0) line integrated intensity to the visual extinction. *Bottom, right panel:* joint distribution of this ratio as a function of the far UV illumination. The horizontal white line corresponds to the standard value of the X_{CO} factor. The blue, green, orange, and red vertical dashed lines show the far UV illumination limits (4, 10, 26, and 120, respectively), which corresponds to the dust temperature limits used in the masks of Fig. 8. The color scales of the two images show the same ranges as the axes of the bottom right joint distribution.

GMCs (Heyer & Dame 2015). While the local values of N_{H}/A_v and X_{CO} are uncertain, and they could well be different from their standard values in Orion B, here we wish to study Orion B as if it was observed from nearby galaxies. In these studies, standard values are used when the metallicity is similar to that of the Milky Way (e.g., see the PAWS project Schinnerer et al. 2013; Pety et al. 2013). From a practical viewpoint, we thus proceeded with standard values, knowing that the correct result is probably in between the CO-traced and dust-traced masses, surface densities, and volume densities.

Enhanced far-UV fields heat large masses of CO gas that turns over-luminous with respect to the standard X_{CO} factor, that is, the average behavior of the CO gas in our Milky way (Planck Collaboration XIX 2011). This effect could compensate for the presence of CO-dark gas (Wolfire et al. 2010; Planck and Fermi Collaborations Int. XXVIII 2015), as proposed by Liszt & Pety (2012) with different observations. Therefore the standard value of X_{CO} may well be applicable to galaxies with a higher than average, yet moderate, massive star-formation rate. A straightforward test would be to increase the

Table 12. Critical density, and percentage of total flux originating from gas in filaments and dense cores for each line.

Species	Transition	n_{crit} cm $^{-3}$	$F_{6 \leq A_v < 15}$ % of F_{tot}	$F_{15 \leq A_v}$ % of F_{tot}
^{12}CO	1–0	2×10^3	38	7.6
^{13}CO	1–0	2×10^3	45	15
HCO^+	1–0	2×10^5	40	16
C_2H	1–0	1×10^5	37	17
c- C_3H_2	2–1	1×10^6	38	17
HCN	1–0	3×10^6	44	18
^{12}CN	1–0	3×10^5	45	19
C^{17}O	1–0	2×10^3	43	26
HNC	1–0	4×10^5	41	27
C^{18}O	1–0	2×10^3	48	29
^{32}SO	2–1	2×10^5	44	31
^{12}CS	2–1	2×10^5	42	32
CH_3OH	2–1	3×10^4	41	48
H^{13}CO^+	1–0	2×10^5	34	56
N_2H^+	1–0	2×10^5	17	88

Notes. The lines are sorted by increasing value of $F_{15 \leq A_v}/F_{\text{tot}}$ (last column). The typical volume density of the regions with $6 \leq A_v < 15$, and $15 \leq A_v$ are 1500, and $7300 \text{ H}_2 \text{ cm}^{-3}$, respectively.

size of the mapped FoV to the full Orion B cloud to test at which scale the CO and dust-traced masses derived with standard values of X_{CO} and the N_{H}/A_v ratio get reconciled to better than a factor of three. Complementary CII observations would also help to settle this point (Goicoechea et al. 2015).

7.3. Dense gas tracers

The brightness of a molecular line depends on the column density of the species, which is affected by the chemistry, and the excitation properties of the line. These in turn depend on the physical properties of the gas (density, temperature, ionization fraction, etc.). Indeed, two conditions must be satisfied for a line to be detected. First, the molecule has to be abundant enough, and second, the excitation conditions must be favorable for the line to be excited and produce bright line emission. It is therefore often assumed that lines with high critical densities, such as the (1–0) lines of HCN and HCO^+ , are good tracers of dense gas because these species are abundant and their emission is only expected to be seen in regions where the density is high enough to excite the line. Table 12 lists the critical density of each molecular line as well as the percentage of total flux that is emitted from regions of intermediate ($6 \leq A_v < 15$) and high ($15 \leq A_v$) visual extinction, as measured in Sect. 4.1. These two regimes are representative of the gas arising in filaments and dense cores, respectively. We do not find any clear correlation between the critical density of the lines and the percentage of flux emitted.

For instance, the lines of the CO isotopologues have nearly equal critical densities (that is, similar excitation conditions) but the percentage of flux coming from the densest regions ($n_{\text{H}_2} \sim 7300 \text{ cm}^{-3}$) varies from 8% for ^{12}CO (1–0) to 29% for C^{18}O (1–0). The higher fraction of flux coming from high-density regions for the rarer isotopologues is the result of both sensitivity and chemistry. The intrinsic lower abundance of ^{13}CO , C^{18}O and C^{17}O compared to the main isotope will result in weaker emission for the rarer isotopologues everywhere in the cloud. Also, in the UV-illuminated layers, ^{12}CO will survive longer than the

Table 13. Flux ratios in nearby galaxies and in Orion B.

Source	HCN/HCO ⁺	¹² CO/HCN	¹² CO/HCO ⁺	¹² CO/N ₂ H ⁺	¹² CN/HCN	C ₂ H/ ¹³ CO	HCN/HNC	Observ.	Ref.
ULIRGs	1.5–2.4	6.3–8.6	9.7–21	40	0.4–0.5	0.8–1.4	1.4–3.0	MOPRA-22 m	1
M 51 P2	1.2	32	39	225	0.5	0.04	2.7	IRAM-30 m	2
AGNs	0.8–2.0	3.4–25	5.7–20	41–68	0.9–1.6	0.2–0.7	2.2–3.0	IRAM-30 m	3
Starbursts	0.7–1.2	16–23	16–24	100–325	1.2–1.4	0.2–0.7	1.9–2.5	IRAM-30 m	3
M 82	0.5	–	–	–	–	–	–	CARMA	4
NGC 253 P7	1.2	6.0	7.0	–	0.6	–	–	ALMA	5
Maffei2B	0.6	–	–	–	–	–	4.3	BIMA, OVRO	6
LMC	0.4–0.7	11–120	6.0–48	59–167	0.2–0.3	0.03–0.27	1.1–3.4	IRAM-30 m	7
Orion B	0.9	39	37	900	0.5	0.05	3.5	IRAM-30 m	8

Notes. ⁽¹⁾ Nishimura et al. (2016); ⁽²⁾ Watanabe et al. (2014); ⁽³⁾ Aladro et al. (2015); ⁽⁴⁾ Salas et al. (2014); ⁽⁵⁾ Meier et al. (2015); ⁽⁶⁾ Meier & Turner (2012); ⁽⁷⁾ Nishimura et al. (2016). ⁽⁸⁾ This work.

CO isotopologues due its capacity to self-shield (process known as selective photo dissociation), although this effect is probably not resolved by the observations.

Lines with much higher critical densities ($>10^5 \text{ cm}^{-3}$) than CO (1–0) ($\sim 10^3 \text{ cm}^{-3}$), such as HCO⁺, HCN, and HNC (1–0), which are expected to trace dense gas, emit only 16, 18, and 27% of their total flux in mapped Orion B regions of high density. Most of the emission then arises in lower density gas. Shirley (2015) extensively discusses the relevance of the notion of critical density. He highlights that the critical density is the density at which collisional de-excitation equals the net radiative emission. He emphasizes that it is computed in the optically thin limit, implying that it is only an upper limit in the presence of photon-trapping. The fact that these lines can be excited and thus detected in diffuse gas was, in addition, recently discussed by Liszt & Pety (2016). While their results cannot be quantitatively applied to the observed FoV because the line peak intensities are slightly outside the range of applicability of the weak excitation regime, the underlying physical process is still present. At the limit of detectability, Liszt & Pety (2016) showed that the intensity of low-energy rotational lines of strongly polar molecules, such as HCO⁺ and HNC, is proportional to the product of the total gas density and the molecule column density, independent of the critical density, as long as the line intensity does not increase above a given value. This implies that for any given gas density there is a column density that will produce an observable line intensity. In the observed field of Orion B, we are in an intermediate radiative transfer regime where the fundamental lines of HCO⁺, HCN, and HNC can be excited in regions of density much smaller than their critical densities.

The lines with the largest fraction of their emission arising in the densest gas are CH₃OH and N₂H⁺. In particular, N₂H⁺ (1–0) that presents a high critical density similar to that of HCO⁺, HCN, and HNC (1–0), has the highest proportion of its flux coming from the densest regions (88%). Moreover, in contrast to all the other lines, only 17% of the total N₂H⁺ (1–0) flux is associated with regions of intermediate A_V ($6 \leq A_V < 15$) which have typical densities of $\sim 1500 \text{ cm}^{-3}$. This shows that the N₂H⁺ (1–0) line is the best molecular tracer of dense regions among the lines studied in this paper.

Despite the similar critical densities between N₂H⁺ and HCO⁺, their behavior is completely different. First, N₂H⁺ is detected over only 2.4% of the observed FoV, while HCO⁺ emission covers 68% of the field. Second, the percentages of the flux coming from dense/translucent regions are 88/8% for N₂H⁺, and 15/41% for HCO⁺. These differences can only be

understood by their different chemistry. HCO⁺ can be formed from ion-molecule reactions involving C⁺ and other cations, notably CH₂⁺ and CH₃⁺, in addition to the protonation of CO. On the contrary, the sole reaction producing N₂H⁺ is the protonation of N₂. Furthermore, the destruction of HCO⁺ by dissociative recombination with electrons produces CO while N₂H⁺ can react with CO to produce HCO⁺. Hence, N₂H⁺ only survives in regions where the electron abundance is low (to prevent dissociative recombination) and where CO is frozen on dust grains (to prevent proton transfer to CO), that is, in cold and dense cores.

In summary, species that have a chemical reason to only be present in dense gas are the only really reliable high density tracers. More generally, the knowledge of the chemical behavior is fundamental in understanding how molecular species can be used to trace the different physical environments.

7.4. Typical line ratios in Orion B and other galaxies

Molecular line ratios have the potential to be powerful probes of physical properties related to star formation activity. Thanks to current observing capabilities, many unbiased line surveys have recently been carried out toward nearby galaxies, and more than 27 species have been detected in the 3 mm band (Meier & Turner 2012; Salas et al. 2014; Watanabe et al. 2014; Aladro et al. 2015; Meier et al. 2015; Nishimura et al. 2016). Common line ratios include the HCN(1–0)/HCO⁺(1–0), ¹²CO(1–0)/HCN(1–0), HCN(1–0)/HNC(1–0) and the CN(1–0)/HCN(1–0), which are proposed tracers of density, temperature and radiation field, respectively.

Figure 23 shows observed line ratios in nearby galaxies and in the Orion B molecular cloud. The comparison includes line ratios obtained with both single-dish telescopes and interferometers, and galaxies with distances between 3.3 and 170 Mpc, in addition to the LMC, the nearest external galaxy (50 kpc). The sample therefore spans two orders of magnitude in spatial resolution (written at the bottom of the y-axis in units of pc). To ease the comparison with Orion B, the ratios are normalized by the Orion B ratios of the lines integrated over the full observed FoV (that is, at a resolution of 10 pc).

Line ratios observed in Orion B are, in general, comparable to what is observed in nearby galaxies. Noticeably, line ratios (except ¹²CO/N₂H⁺) in Orion B at a resolution of 10 pc are very similar to those observed at a resolution of 1000 pc in the spiral arm of the famous whirlpool galaxy (M 51), a prototype of grand design spiral galaxy.

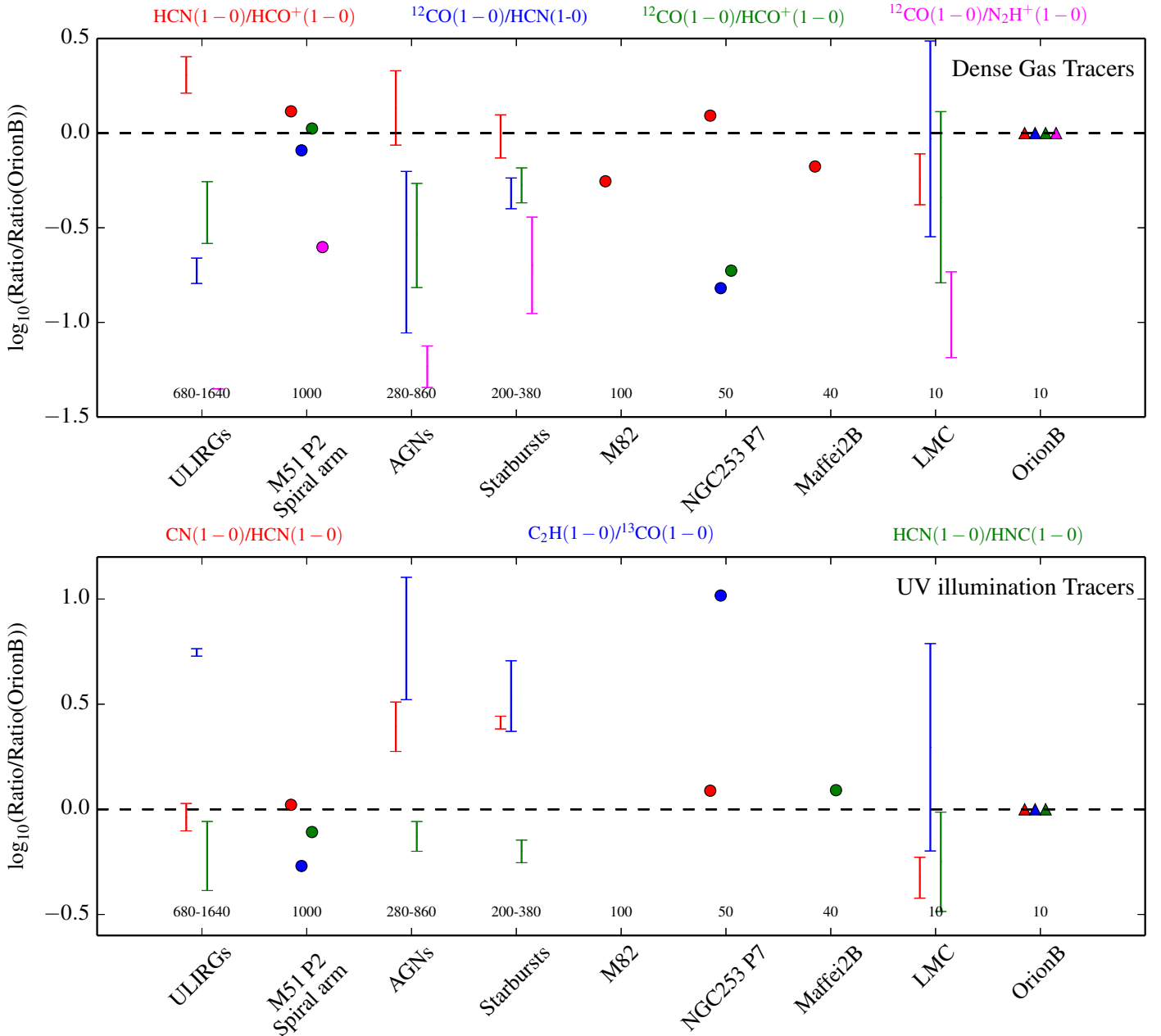


Fig. 23. Line ratios observed towards nearby galaxies and the Orion B molecular cloud. The *upper and lower panels* include line ratios which are proposed dense gas and UV-illumination tracers, respectively. A point is plotted for individual measures, while a range of values is given for the Ultra-Luminous Infra-Red Galaxies (ULIRG), Active Galactic Nuclei (AGN), and starburst samples, which contain measures for several galaxies. The ULIRGs include Arp 220 and Mrk 231, while AGNs include M 51, NGC 1068 and NGC 7469, and the starburst galaxies include M 83, NGC 253 and M 82. The sources are sorted by decreasing spatial resolution, which is given at the bottom of the figure for each source. The Orion B values correspond to the ratios of the lines integrated over the full region to simulate a 10 pc spatial resolution allowing a better comparison with the other galaxies.

The HCN/HCO⁺ ratio (shown in red in the upper panel) is assumed to trace dense gas that will eventually form stars, and thus is often used to trace the star formation activity in other galaxies. Both lines are among the brightest lines observed and are thus easily detected. ULIRGs and AGNs present the largest HCN/HCO⁺ ratios, but there are no major differences between the sources. The resolved spatial distribution in Orion B (see Fig. 19) shows that in the case of UV-illuminated gas, the HCN/HCO⁺ ratio does not trace the high-density gas. Another proposed tracer of dense gas is the inverse of the ¹²CO/HCN ratio (shown in blue in the upper panel). This ratio is higher in Orion B, the LMC and in the spiral arm of M 51 than in

the other galaxies. The ¹²CO/HCO⁺ ratio behaves in a similar way. While the resolved spatial distribution in Orion B (see Fig. 14) shows that these ratios actually separate diffuse from dense gas, the quantitative analysis shows that HCO⁺ and HCN (1–0) fluxes mostly trace densities around 500–1500 H₂ cm⁻³ instead of $\sim 10^4$ cm⁻³.

Better tracers of high-density gas are ratios involving N₂H⁺, such as CO(1–0)/N₂H⁺(1–0) (shown in magenta), because N₂H⁺ resides solely in dense gas ($> 10^4$ cm⁻³), contrary to HCN that can be present at lower densities (see Sect. 4.1). Starbursts (including M 51) and ULIRGs form many stars, requiring the presence of many dense cores, and thus a high N₂H⁺ (1–0)

brightness relative to ^{12}CO (1–0) that traces the total reservoir of molecular gas. In contrast, Orion B has a low star-formation efficiency (Lada et al. 2010; Megeath et al. 2016), probably implying a low number of dense cores and thus a lower relative N_2H^+ brightness. The low surface filling factor of N_2H^+ makes it difficult to detect at high signal-to-noise ratio with single-dish telescopes in external galaxies. Fortunately, the much better resolving power of NOEMA and ALMA relieves this difficulty and N_2H^+ starts to be detected in nearby galaxies.

The HCN/HNC is another popular line ratio measured in nearby galaxies (shown in green in the bottom panel). Both species are abundant in cold clouds, but at temperatures higher than approximately 30 K, HNC starts to be converted to HCN through reactions with H (see, e.g., Schilke et al. 1992; Graninger et al. 2014). The HCN/HNC ratio is thus increasing at higher temperatures. The sources included in this comparison present similar HCN/HNC ratios within a factor of two. The spatial distribution shown in Fig. 19 is consistent with the proposed temperature dependence of this ratio, whose lowest values are found in the cold filaments, and which correlates well with the map of the dust temperature seen in Fig. 2.

Finally, the CN/HCN intensity ratio (shown in red in the bottom panel) is expected to trace UV-illuminated gas because CN is a major product of HCN photodissociation. Indeed, higher abundance ratios are found in PDRs and XDRs compared to cold dark clouds (Fuente et al. 2005; Baan et al. 2008). However, in spatially resolved observations, there is no clear correlation of the CN/HCN flux ratio with radiation field (see Fig. 19). Furthermore, in our comparison, AGNs and starbursts present the largest CN/HCN ratios, and ULIRGs have similar ratios to the Orion B cloud and the spiral arm of M51. This is contradictory with CN/HCN being a radiation field tracer. In fact, the ratios that involve the HCN (1–0) line must be taken with care because this line is known to be pumped by IR photons (Aalto et al. 2007). This will produce brighter HCN lines, and thus could explain the low CN/HCN ratio observed in ULIRGs. A better tracer of radiation field is the $\text{C}_2\text{H}(1-0)/^{13}\text{CO}(1-0)$ ratio. Carbon chains, such as C_2H and C_3H_2 , have been observed to form efficiently in UV-illuminated regions (Pety et al. 2005; Guzmán et al. 2015). ULIRGs, AGNs and starburst galaxies present the largest $\text{C}_2\text{H}/^{13}\text{CO}$ ratios, consistent with their high star-formation activities. Moreover, the spatial distribution of the $\text{C}_2\text{H}/^{13}\text{CO}$ ratio (see Fig. 15) shows a clear gradient between the illuminated edge (right) and the UV-shielded (left) side of the Orion B molecular cloud. Therefore, the $\text{C}_2\text{H}(1-0)/^{13}\text{CO}(1-0)$ ratio is a potential tracer of the presence of massive stars.

8. Conclusion

The ORION-B project aims at imaging a statistically significant fraction of the Orion B GMC over the 3 mm atmospheric window, starting with approximately one square degree towards NGC 2024, NGC 2023, Horsehead, and IC 434. The mean dust temperature in the mapped region is 26 K, and the probability distribution function of the visual extinction shows a wide distribution of magnitudes, from less than 1 to a few 100, with most of the surface and volume lying below a magnitude of 15. These dust properties suggests that the south-western edge of Orion B is permeated by far-UV fields from massive stars at relatively large spatial scales. Most of the cloud mass is contained in regions of relatively low A_V , implying that photon-dominated regions are everywhere in the FoV. This is the reason why CO

is over-luminous, resulting in a CO-traced mass that is approximately three time as much as the dust traced mass in this region.

Over the 84 to 116 GHz frequency range, we easily detected the fundamental lines of CO isotopologues (from ^{12}CO to C^{17}O), HCO^+ , HCN, HNC, and their ^{13}C isotopologues, ^{12}CN , C_2H , and N_2H^+ , as well as higher J lines of ^{12}CS , ^{32}SO , SiO , $\text{c-C}_3\text{H}_2$, and methanol. The faintest averaged spectra of the species presented in this article, the spectra of HN^{13}C (1–0), is \sim 2400 fainter than ^{12}CO (1–0) line. Still fainter lines, tentatively detected in the averaged spectra, are present. They will be discussed in a future paper.

The main CO isotopologues and a number of other species clearly display two velocity components: the main component centered at \sim 10 km s $^{-1}$, where most of the gas lies, and a more diffuse component centered at \sim 5 km s $^{-1}$ that contains approximately 10% of the molecular gas along the line of sight. Tomography studies of the interstellar medium using visible absorption against background stars indicates that both components belong to Orion B; their relative distance is compatible with the projected extension of Orion B.

A significant fraction of the HCO^+ , HCN, and HNC (1–0) flux integrated over the observed FoV is coming from translucent (41, 36, and 29%, respectively) and from gas forming the filamentary structure (typically 40–45%). Only 16, 18, and 29% (for HCO^+ , HCN, and HNC, respectively) of the flux is coming from dense cores ($A_V > 15$). The common assumption that lines of large critical densities (\sim 10 5 cm $^{-3}$) can only be excited by gas of similar density is clearly incorrect. Another unrelated result is that these lines are also sensitive to the amount of far-UV illumination, even though less sensitive than the fundamental line of small hydrocarbon chains and ^{12}CN .

While the HCO^+ and N_2H^+ (1–0) lines have similar critical densities and similar peak temperatures over the mapped FoV, the repartition of their flux has a completely different behavior: The N_2H^+ (1–0) line is only emitted from regions with $A_V > 15$, while the HCO^+ (1–0) line is also emitted from regions of visual extinction as low as 1–2 mag. This explains why the surface filling factor of detected emission highly differs between these two species. This is in part due to the fact that there exists another regime of radiative transfer (the weak excitation limit) that produces detectable lines of strongly polar molecules (Liszt & Pety 2016, and reference therein). The difference of behavior between HCO^+ and N_2H^+ can easily be explained by the way these molecules are produced and destroyed in diffuse and dense gas.

We observe a strong correlation of the line integrated intensities with A_V , that is, the line strength increases with the quantity of material along the line of sight. This correlation will be quantified in Gratier et al. (2017) through a PCA that allows us to find significant correlations beyond this one with other physical parameters, such as UV illumination. However, the best tracers of the column density are the C^{18}O and HNC (1–0) lines, followed by the ^{12}CS (2–1) line. This validates the use of these lines to normalize the intensities in extra-galactic studies. The different species clearly show A_V threshold values above which they start to emit. Dividing the line integrated intensities by the visual extinction enables us to remove this correlation and to bring forward chemical differences between the species.

When the visual extinction is not available, making the ratio of the line integrated intensities also emphasizes different chemistry behavior. However, proposed dense-gas tracers such as the HCN(1–0)/ HCO^+ (1–0) or HCN(1–0)/ ^{12}CO (1–0) line ratios should be superseded by N_2H^+ (1–0)/ ^{12}CO (1–0) that more accurately traces the fraction of dense gas (\gtrsim 10 4 cm $^{-3}$). The fact

that the CN(1–0)/HCN(1–0) line ratio has a pretty flat spatial distribution in our FoV, may be because the gas is permeated by far-UV fields. However, we find that the C₂H(1–0)/¹³CO(1–0) line ratio is an excellent tracer of the variations of the far-UV illumination in our FoV.

The increasing capabilities of millimeter receivers make it possible to observe multiple molecular lines in large FoVs, and thus to use the spatial distribution of low- J line ratios to classify each line of sight depending on its molecular content.

Acknowledgements. We thank the referee, J. G. Mangum, for his careful reading of the manuscript and useful comments that improved the article. We thank R. Lallement for useful discussions about the distance of the gas in Orion B. We thank P. Andre and N. Schneider for giving us access to the *Herschel* Gould Belt Survey data, and M. Lombardi for delivering his fit of the spectral energy distribution of the *Herschel* data. We thank CIAS for their hospitality during the two workshops devoted to this project. This work was supported by the CNRS program “Physique et Chimie du Milieu Interstellaire” (PCMI). J.R.G. thanks MINECO, Spain, for funding support under grant AYA2012-32032. V.V.G. thanks for support from the Chilean Government through the Becas Chile program. P.G.’s postdoctoral position was funded by the INSU/CNRS. P.G. thanks ERC starting grant (3DICE, grant agreement 336474) for funding during this work. NRAO is operated by Associated Universities Inc. under contract with the National Science Foundation. This paper is based on observations carried out at the IRAM-30 m single-dish telescope. IRAM is supported by INSU/CNRS (France), MPG (Germany) and IGN (Spain). This research also used data from the *Herschel* Gould Belt survey (HGBS) project (<http://gouldbelt-herschel.cea.fr>). The HGBS is a *Herschel* Key Programme jointly carried out by SPIRE Specialist Astronomy Group 3 (SAG 3), scientists of several institutes in the PACS Consortium (CEA Saclay, INAF-IFSI Rome and INAF-Arcetri, KU Leuven, MPIA Heidelberg), and scientists of the *Herschel* Science Center (HSC).

References

- Aalto, S., Spaans, M., Wiedner, M. C., & Hüttemeister, S. 2007, *A&A*, **464**, 193
 Abergel, A., Bernard, J. P., Boulanger, F., et al. 2002, *A&A*, **389**, 239
 Aladro, R., Martín, S., Riquelme, D., et al. 2015, *A&A*, **579**, A101
 André, P., Men'shchikov, A., Bontemps, S., et al. 2010, *A&A*, **518**, L102
 Anthony-Twarog, B. J. 1982, *AJ*, **87**, 1213
 Baan, W. A., Henkel, C., Loenen, A. F., Baudry, A., & Wiklind, T. 2008, *A&A*, **477**, 747
 Bergin, E. A., & Tafalla, M. 2007, *ARA&A*, **45**, 339
 Bigiel, F., Leroy, A. K., Jiménez-Donaire, M. J., et al. 2016, *ApJ*, **822**, L26
 Bik, A., Lenorzer, A., Kaper, L., et al. 2003, *A&A*, **404**, 249
 Bohllin, R. C., Savage, B. D., & Drake, J. F. 1978, *ApJ*, **224**, 132
 Bolatto, A. D., Wolfire, M., & Leroy, A. K. 2013, *ARA&A*, **51**, 207
 Cardelli, J. A., Clayton, G. C., & Mathis, J. S. 1989, *ApJ*, **345**, 245
 Chernin, L. M. 1996, *ApJ*, **460**, 711
 Fabricius, C., Bastian, U., Portell, J., et al. 2016, *A&A*, **595**, A3
 Federrath, C., & Klessen, R. S. 2012, *ApJ*, **761**, 156
 Federrath, C., & Klessen, R. S. 2013, *ApJ*, **763**, 51
 Frerking, M. A., Langer, W. D., & Wilson, R. W. 1982, *ApJ*, **262**, 590
 Fuente, A., García-Burillo, S., Gerin, M., et al. 2005, *ApJ*, **619**, L155
 Gaia Collaboration (Brown, A. G. A., et al.) 2016a, *A&A*, **595**, A2
 Gaia Collaboration (Prusti, T., et al.) 2016b, *A&A*, **595**, A1
 Goicoechea, J. R., Teyssier, D., Etxaluze, M., et al. 2015, *ApJ*, **812**, 75
 Graninger, D. M., Herbst, E., Öberg, K. I., & Vasyunin, A. I. 2014, *ApJ*, **787**, 74
 Gratier, P., Bron, E., Gerin, M., et al. 2017, *A&A*, **599**, A100
 Green, G. M., Schlaflly, E. F., Finkbeiner, D. P., et al. 2015, *ApJ*, **810**, 25
 Guzmán, V. V., Pety, J., Goicoechea, J. R., et al. 2015, *ApJ*, **800**, L33
 Habing, H. J. 1968, *Bull. Astron. Inst. Netherlands*, **19**, 421
 Hennebelle, P. 2013, *A&A*, **556**, A153
 Hennebelle, P., & Chabrier, G. 2011, *ApJ*, **743**, L29
 Heyer, M., & Dame, T. M. 2015, *ARA&A*, **53**, 583
 Hollenbach, D. J., Takahashi, T., & Tielens, A. G. G. M. 1991, *ApJ*, **377**, 192
 Hughes, A., Meidt, S. E., Colombo, D., et al. 2013, *ApJ*, **779**, 46
 Hummel, C. A., Rivinius, T., Nieva, M.-F., et al. 2013, *A&A*, **554**, A52
 Kalberla, P. M. W., Burton, W. B., Hartmann, D., et al. 2005, *A&A*, **440**, 775
 Kim, C.-G., Ostriker, E. C., & Kim, W.-T. 2013, *ApJ*, **776**, 1
 Lada, C. J., Lombardi, M., & Alves, J. F. 2010, *ApJ*, **724**, 687
 Lada, C. J., Forbrich, J., Lombardi, M., & Alves, J. F. 2012, *ApJ*, **745**, 190
 Lada, C. J., Lombardi, M., Roman-Zuniga, C., Forbrich, J., & Alves, J. F. 2013, *ApJ*, **778**, 133
 Lallement, R., Vergely, J.-L., Valette, B., et al. 2014, *A&A*, **561**, A91
 Leroy, A. K., Hughes, A., Schruba, A., et al. 2016, *ApJ*, **831**, 16
 Lindegren, L., Lammers, U., Bastian, U., et al. 2016, *A&A*, **595**, A4
 Liszt, H., & Lucas, R. 2001, *A&A*, **370**, 576
 Liszt, H. S., & Pety, J. 2012, *A&A*, **541**, A58
 Liszt, H. S., & Pety, J. 2016, *ApJ*, **823**, 124
 Lombardi, M., Bouy, H., Alves, J., & Lada, C. J. 2014, *A&A*, **566**, A45
 Lucas, R., & Liszt, H. 1996, *A&A*, **307**, 237
 Lucas, R., & Liszt, H. S. 2000, *A&A*, **358**, 1069
 Mangum, J. G., Emerson, D. T., & Greisen, E. W. 2007, *A&A*, **474**, 679
 Marsh, K. A., Griffin, M. J., Palmeirim, P., et al. 2014, *MNRAS*, **439**, 3683
 Megeath, S. T., Gutermuth, R., Muzerolle, J., et al. 2016, *AJ*, **151**, 5
 Meidt, S. E., Schinnerer, E., García-Burillo, S., et al. 2013, *ApJ*, **779**, 45
 Meier, D. S., & Turner, J. L. 2012, *ApJ*, **755**, 104
 Meier, D. S., Walter, F., Bolatto, A. D., et al. 2015, *ApJ*, **801**, 63
 Menten, K. M., Reid, M. J., Forbrich, J., & Brunthaler, A. 2007, *A&A*, **474**, 515
 Nishimura, Y., Shimonishi, T., Watanabe, Y., et al. 2016, *ApJ*, **818**, 161
 Orkisz, J. H., Pety, J., Gerin, M., et al. 2017, *A&A*, **599**, A99
 Penzias, A. A., & Purcell, C. A. 1973, *ARA&A*, **11**, 51
 Pety, J. 2005, in SF2A-2005: in Semaine de l’Astrophysique Française, eds. F. Casoli, T. Contini, J. M. Hameury, & L. Pagani, 721
 Pety, J., Teyssier, D., Fossé, D., et al. 2005, *A&A*, **435**, 885
 Pety, J., Bardeau, S., & Reynier, E. 2009, IRAM-30 m EMIR time/sensitivity estimator, Tech. Rep., iRAM Memo 2009-1
 Pety, J., Schinnerer, E., Leroy, A. K., et al. 2013, *ApJ*, **779**, 43
 Planck Collaboration I. 2011, *A&A*, **536**, A1
 Planck Collaboration XIX. 2011, *A&A*, **536**, A19
 Planck and Fermi Collaborations Int. XXVIII. 2015, *A&A*, **582**, A31
 Richer, J. S. 1990, *MNRAS*, **245**, 24P
 Rieke, G. H., & Lebofsky, M. J. 1985, *ApJ*, **288**, 618
 Salas, P., Galaz, G., Salter, D., et al. 2014, *ApJ*, **797**, 134
 Sandell, G., Avery, L. W., Baas, F., et al. 1999, *ApJ*, **519**, 236
 Schaefer, G. H., Hummel, C. A., Gies, D. R., et al. 2016, *AJ*, **152**, 213
 Schilke, P., Walmsley, C. M., Pineau Des Forets, G., et al. 1992, *A&A*, **256**, 595
 Schinnerer, E., Meidt, S. E., Pety, J., et al. 2013, *ApJ*, **779**, 42
 Schlaflly, E. F., Green, G., Finkbeiner, D. P., et al. 2014, *ApJ*, **786**, 29
 Schneider, N., André, P., Könyves, V., et al. 2013, *ApJ*, **766**, L17
 Shetty, R., Kauffmann, J., Schnee, S., Goodman, A. A., & Ercolano, B. 2009, *ApJ*, **696**, 2234
 Shirley, Y. L. 2015, *PASP*, **127**, 299
 Solomon, P. M., Rivolo, A. R., Barrett, J., & Yahil, A. 1987, *ApJ*, **319**, 730
 Spitzer, L. 1978, Physical processes in the interstellar medium (New York: Wiley-Interscience)
 van Leeuwen, F. 2007, *A&A*, **474**, 653
 Watanabe, Y., Sakai, N., Sorai, K., & Yamamoto, S. 2014, *ApJ*, **788**, 4
 Wolfire, M. G., Hollenbach, D., & McKee, C. F. 2010, *ApJ*, **716**, 1191

Appendix A: Noise properties

Table A.1 summarizes the single-dish observations described in Sect. 2.2. Figure A.1 shows the average system temperature as a function of the rest frequency over the observed bandwidth. The mean (solid line) was computed over all the calibration measurements made during the observation and the shaded backgrounds display the $\pm 3\sigma$ interval that reflects both variations in the quality of the tuning and of the elevation of the source. The variations with the frequency come from a combination of hardware and atmosphere chromaticity effects. The optic and mixer performances vary with the observed radio-frequency and the cryogenic low noise amplifier performances vary with the instantaneous intermediate frequency. The atmospheric transparency mostly varies because of ozone lines present in the bandpass and because of the 118.75 GHz ($N = 1-1, J = 1-0$) oxygen line whose wings strongly increase the T_{sys} at the upper end of the 3 mm atmospheric window.

Figure A.2 shows the spatial distribution of the noise at an angular resolution of $31''$ for two lines, each one representing one of the two tunings. The regions around the Horsehead and NGC 2023 were observed at the start of the project, before our observing strategy converged to the one described in Sect. 2.2. In particular, this area was covered at least once along the δx axis, and once along the δy axis. This explains why the noise properties of this region are different from other parts of the map. Except for this part of the map, the variations in the noise level reflect the variations of weather or elevation during the observations.

Appendix B: Mean line profiles from different gas regimes

In Sect. 4, we derived the fraction of fluxes that comes from different gas regimes in the lines averaged over the observed FoV. Here we intend to deliver the tools to estimate the typical line fluxes when varying the number of lines of sight that sample the

different gas regimes. We thus compute the mean line profiles over the same gas regimes as defined in Sects. 4.1 and 4.2. Mixing these line profiles in different proportions would deliver a proxy for the line profile observed in GMCs that have different ratios of diffuse/dense gas or cold/warm gas.

Figures B.1 and B.3 show the mean line profiles for the different A_V and T_d regimes. Tables B.1 and B.2 present, for each transition, line integrated intensity averaged over the different A_V and T_d masked regions. Figures B.2 and B.4 show these line integrated intensities as percentages of the integrated intensity averaged over the full FoV. These later plots indicate the potential intensity gain that can be expected when resolving the regions that are compact.

As expected, the intensity increases with the visual extinction, that is, with the column density of matter. However, the increase is only a factor two for the ^{12}CO ($1-0$) line while it reaches a factor of almost 30 for the N_2H^+ ($1-0$) line. All lines except N_2H^+ ($1-0$) have a mean integrated intensity that increases by a factor of two in the filamentary gas ($6 \leq A_V < 15$). The mean spectra at 10 pc resolution are closer to the mean spectra over the translucent gas for all the lines, except for the H^{13}CO^+ , CH_3OH , and N_2H^+ low- J lines.

The C_2H , c- C_3H_2 , ^{12}CN , ^{12}CO , HCN, and HCO^+ low- J lines have similar mean integrated intensities in regions of cold and hot dust, probably because some of the high visual extinction lines of sight are also associated with high dust temperature. The mean spectra of hot dust regions have significantly wider linewidths than the mean spectra of the cold dust regions, confirming that the gas temperature is significantly higher in at least the PDR parts along these lines of sight. The HNC, ^{13}CO , ^{12}CS , C^{17}O , ^{32}SO , C^{18}O , H^{13}CO^+ , CH_3OH , and N_2H^+ low- J line mean integrated intensities are between 2 and 20 times brighter in the cold than in the hot dust regions. These lines are thus more characteristic of cold dense gas than the previous category. Finally, the mean line integrated intensity over the full FoV is closer to the line intensity integrated over the regions of warm and lukewarm dust regions than over the cold or hot dust regions.

Table A.1. Observation parameters.

Species	Transition	Frequency GHz	Setup	F_{eff}	B_{eff}	T_{sys} K	Beam ^a ''	Vel. res. ^b km s ⁻¹	Int. time ^c hr	Noise ^d K
¹² CO	1-0	115.271202	110/USB	0.95	0.78	287	22.5/31	0.51/0.5	40.4/62.4	0.49/0.18
CN	1-0	113.490970	110/USB	0.95	0.79	188	22.8/31	0.52/0.5	40.4/62.4	0.31/0.11
¹⁷ O	1-0	112.358982	110/USB	0.95	0.79	167	23.1/31	0.52/0.5	40.4/62.4	0.27/0.10
¹³ CO	1-0	110.201354	110/USB	0.95	0.79	118	23.5/31	0.53/0.5	40.4/62.4	0.17/0.07
¹⁸ O	1-0	109.782173	110/USB	0.95	0.79	114	23.6/31	0.53/0.5	40.4/62.4	0.17/0.07
³² SO	2-1	99.299870	110/LSB	0.95	0.80	95	26.1/31	0.59/0.5	40.4/62.4	0.13/0.06
¹² CS	2-1	97.980953	110/LSB	0.95	0.80	90	26.5/31	0.60/0.5	40.4/62.4	0.12/0.06
CH ₃ OH-A	2-1	96.741375	110/LSB	0.95	0.81	93	26.8/31	0.60/0.5	40.4/62.4	0.11/0.06
CH ₃ OH-E	2-1	96.739362	110/LSB	0.95	0.81	93	26.8/31	0.60/0.5	40.4/62.4	0.11/0.06
N ₂ H ⁺	1-0	93.173764	110/LSB	0.95	0.81	100	27.8/31	0.63/0.5	40.4/62.4	0.13/0.07
HNC	1-0	90.663568	102/LSB	0.95	0.81	115	28.6/31	0.64/0.5	44.9/70.5	0.12/0.08
HCO ⁺	1-0	89.188525	102/LSB	0.95	0.81	130	29.1/31	0.66/0.5	44.9/70.5	0.13/0.09
HCN	1-0	88.631848	102/LSB	0.95	0.81	124	29.3/31	0.66/0.5	44.9/70.5	0.12/0.09
C ₂ H	1-0	87.316898	102/LSB	0.95	0.82	132	29.7/31	0.67/0.5	44.9/70.5	0.15/0.11
HN ¹³ C	1-0	87.090825	102/LSB	0.95	0.81	137	28.6/31	0.64/0.5	44.9/70.5	0.14/0.11
SiO	2-1	86.846960	102/LSB	0.95	0.82	142	29.9/31	0.67/0.5	44.9/70.5	0.14/0.11
H ¹³ CO ⁺	1-0	86.754288	102/LSB	0.95	0.81	136	28.6/31	0.64/0.5	44.9/70.5	0.14/0.10
H ¹³ CN	1-0	86.340184	102/LSB	0.95	0.81	136	28.6/31	0.64/0.5	44.9/70.5	0.13/0.10
c-C ₃ H ₂	2-1	85.338893	102/LSB	0.95	0.82	123	30.4/31	0.69/0.5	44.9/70.5	0.12/0.10

Notes. ^(a) Listed as natural/smoothed resolution. ^(b) Listed as natural/oversampled channel spacing. ^(c) Listed as on-source time/telescope time. ^(d) Listed as measured on the natural/resampled resolution cubes.

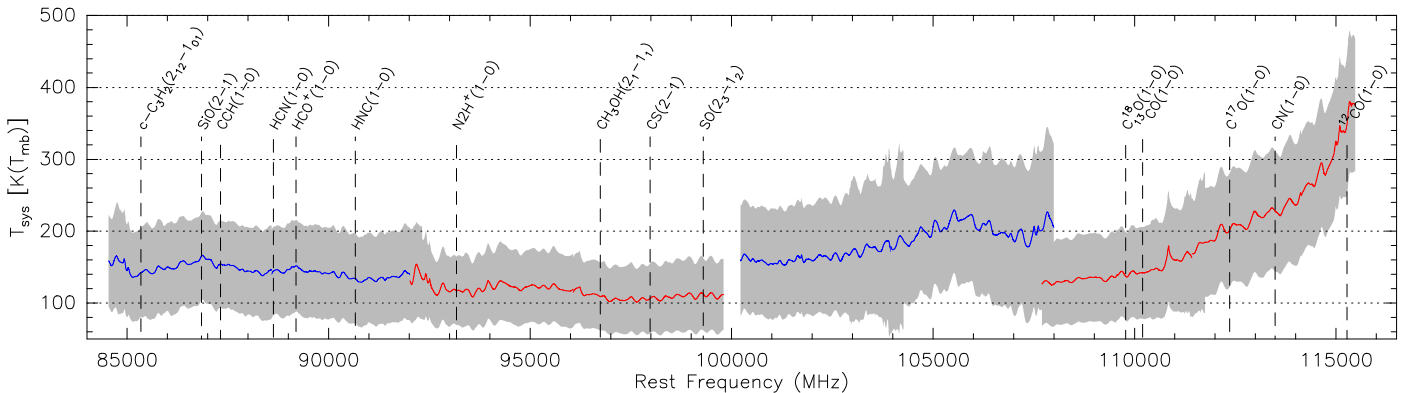


Fig. A.1. T_{sys} as a function of the frequency. The solid lines display the average T_{sys} and the gray shaded backgrounds show the $\pm 3\sigma$ interval at each frequency. The blue and red colors present the instantaneous 8 GHz-bandwidth of the lower and upper sidebands covered by the two tunings. The vertical dashed lines show the frequencies of the brightest lines studied here.

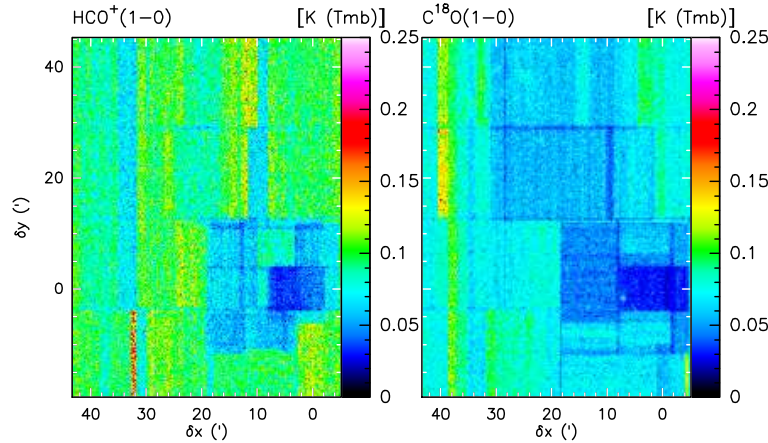


Fig. A.2. Typical spatial distribution of the RMS noise for two lines, each one belonging to one of the two tuning setups.

Table B.1. Line averaged intensities in mK km s⁻¹ and in percentage of the total flux inside the four A_V mask regions.

Species	Transition	$0 \leq A_V < 222$	$1 \leq A_V < 2$	$2 \leq A_V < 6$	$6 \leq A_V < 15$	$15 \leq A_V < 222$
¹² CO	1–0	33 000 (100%)	3300 (9.9%)	36 000 (110%)	65 000 (200%)	77 000 (230%)
¹³ CO	1–0	6200 (100%)	350 (5.7%)	4900 (79%)	15000 (230%)	29 000 (470%)
HCO ⁺	1–0	980 (100%)	110 (11%)	840 (85%)	2000 (210%)	4700 (480%)
HCN	1–0	590 (100%)	40 (6.9%)	440 (75%)	1300 (230%)	3200 (550%)
C ¹⁸ O	1–0	430 (100%)	8.4 (1.9%)	210 (49%)	1100 (240%)	3800 (880%)
¹² CS	2–1	370 (100%)	9.9 (2.7%)	190 (52%)	800 (220%)	3700 (990%)
¹² CN	1–0	350 (100%)	36 (10%)	250 (70%)	810 (230%)	2100 (590%)
HNC	1–0	310 (100%)	26 (8.4%)	190 (61%)	650 (210%)	2600 (830%)
C ₂ H	1–0	270 (100%)	47 (18%)	230 (87%)	510 (190%)	1400 (520%)
³² SO	2–1	200 (100%)	6.8 (3.4%)	100 (50%)	460 (230%)	1900 (940%)
C ¹⁷ O	1–0	100 (100%)	23 (22%)	53 (53%)	230 (220%)	800 (780%)
c-C ₃ H ₂	2–1	87 (100%)	15 (18%)	73 (84%)	170 (190%)	450 (520%)
H ¹³ CO ⁺	1–0	33 (100%)	0.87 (2.6%)	4.9 (15%)	57 (170%)	560 (1700%)
N ₂ H ⁺	1–0	29 (100%)	-13 (-45%)	5 (17%)	25 (85%)	780 (2700%)
CH ₃ OH	2–1	27 (100%)	4.7 (17%)	3.3 (12%)	57 (210%)	390 (1500%)

Notes. The lines are sorted by decreasing value of their intensity.

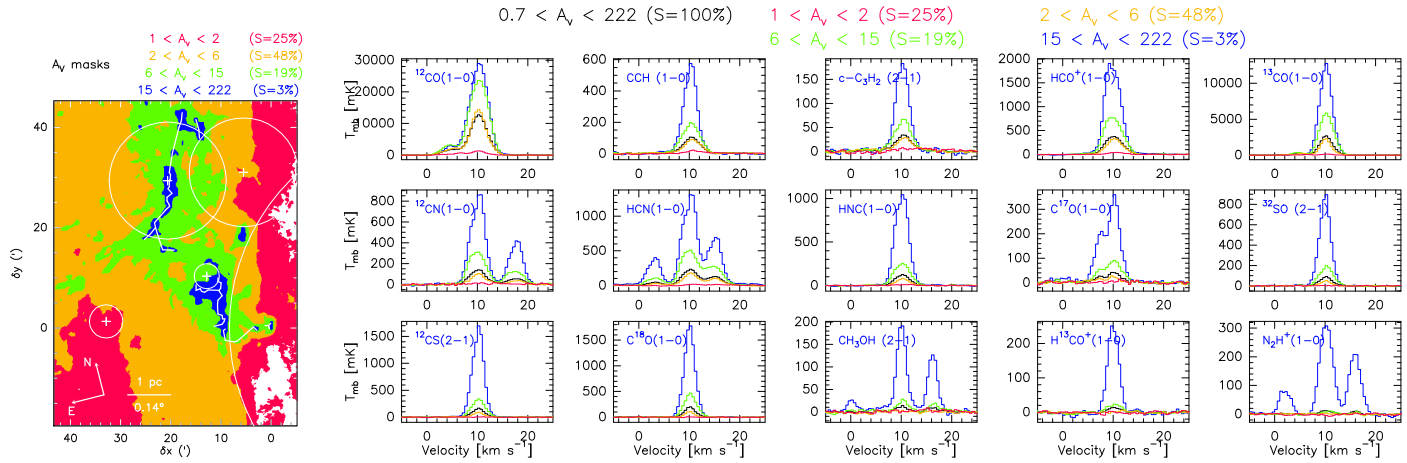


Fig. B.1. Same as Fig. 6, except that the spectra show the temperature intensity averaged over the different masks.

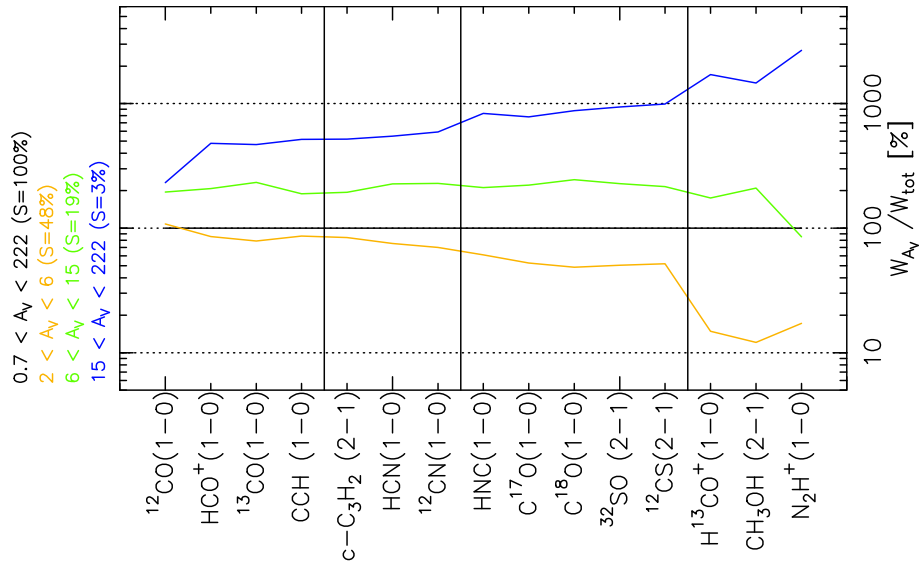


Fig. B.2. For each transition, line integrated intensity computed over the same velocity range divided by the line integrated intensity computed over the surface where $A_V \geq 15$. All line integrated intensities are computed between 9 and 12 km s⁻¹. The black vertical lines define the groups of lines described in Sect. 4.1.

Table B.2. Line intensities averaged over $[9, 12 \text{ km s}^{-1}]$ inside the four T_d mask regions in mK km s^{-1} and in percentage of the intensity of the cold dust region.

Species	Transition	$16 \leq T_d < 100$	$16 \leq T_d < 19.5$	$19.5 \leq T_d < 23.5$	$23.5 \leq T_d < 32$	$32 \leq T_d < 100$
^{12}CO	1–0	33 000 (100%)	44 000 (130%)	28 000 (85%)	31 000 (94%)	56 000 (170%)
^{13}CO	1–0	6200 (100%)	15 000 (250%)	5800 (92%)	5000 (81%)	10 000 (170%)
HCO^+	1–0	980 (100%)	2500 (250%)	670 (68%)	870 (89%)	2200 (220%)
HCN	1–0	590 (100%)	1400 (230%)	390 (66%)	500 (85%)	1500 (250%)
C^{18}O	1–0	430 (100%)	2100 (490%)	420 (99%)	290 (67%)	660 (150%)
^{12}CS	2–1	370 (100%)	1700 (450%)	290 (78%)	250 (69%)	830 (230%)
^{12}CN	1–0	350 (100%)	770 (220%)	220 (61%)	290 (81%)	970 (280%)
HNC	1–0	310 (100%)	1300 (430%)	210 (69%)	240 (79%)	690 (230%)
C_2H	1–0	270 (100%)	460 (170%)	150 (57%)	260 (97%)	670 (250%)
^{32}SO	2–1	200 (100%)	1200 (610%)	170 (84%)	140 (70%)	350 (180%)
C^{17}O	1–0	100 (100%)	440 (430%)	100 (99%)	73 (72%)	150 (140%)
c- C_3H_2	2–1	87 (100%)	200 (230%)	50 (57%)	85 (97%)	210 (240%)
H^{13}CO^+	1–0	33 (100%)	290 (890%)	25 (75%)	19 (58%)	67 (210%)
N_2H^+	1–0	29 (100%)	420 (1500%)	25 (86%)	11 (37%)	44 (150%)
CH_3OH	2–1	27 (100%)	260 (970%)	21 (78%)	19 (72%)	38 (140%)

Notes. The lines are sorted by decreasing value of their intensity.

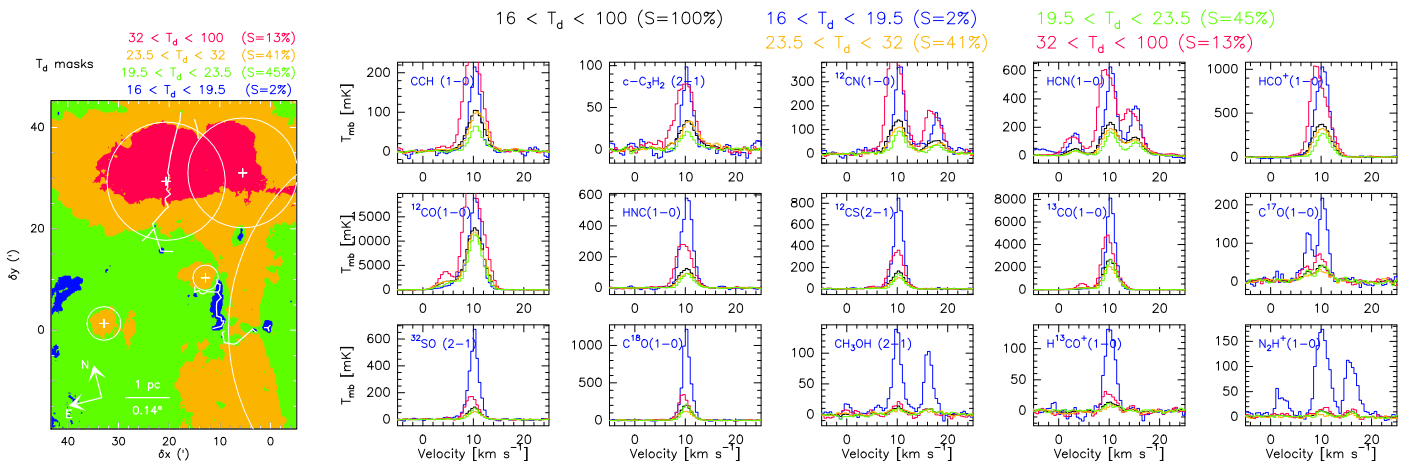


Fig. B.3. Same as Fig. 8, except that the spectra show the temperature intensity averaged over the different masks.

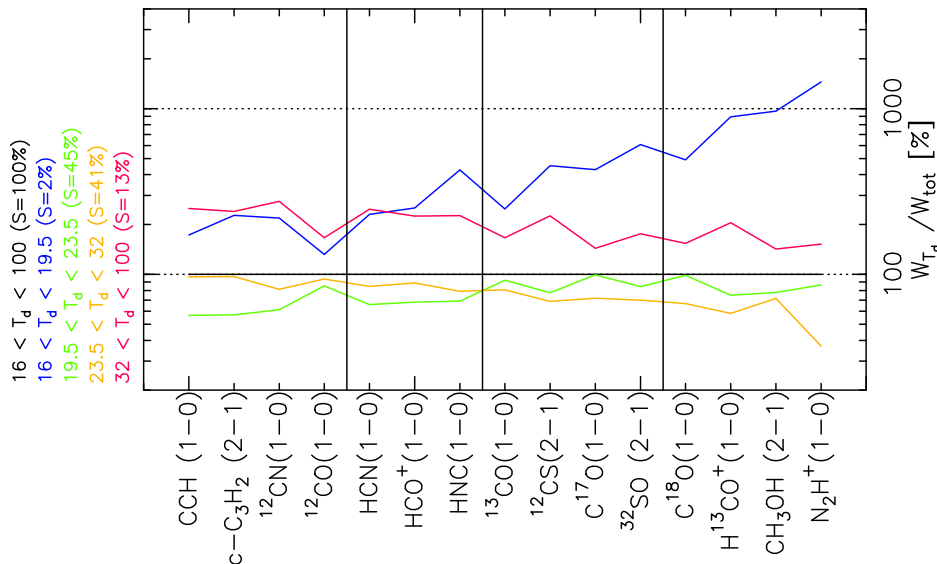


Fig. B.4. For each transition, line integrated intensity divided by the line integrated intensity computed over the surface where $T_d < 20 \text{ K}$. All line integrated intensities are computed between 9 and 12 km s^{-1} . The black vertical lines define the groups of lines described in Sect. 4.2.